HHS Public Access

Author manuscript

Nat Immunol. Author manuscript; available in PMC 2019 September 18.

Published in final edited form as:

Nat Immunol. 2019 April ; 20(4): 407–419. doi:10.1038/s41590-019-0344-y.

Infection drives meningeal engraftment by inflammatory monocytes that impairs CNS immunity

Rejane Rua, **Jane Y. Lee**, **Alexander B. Silva**, **Isabella S. Swafford**, **Dragan Maric**, **Kory R. Johnson**, and **Dorian B. McGavern**

Viral Immunology and Intravital Imaging Section, National Institute of Neurological Disorders and Stroke, National Institutes of Health, Bethesda, Maryland, USA.

Abstract

Tissue macrophages have an embryonic origin and can be replenished in some tissues under steady state conditions by blood monocytes. However, little is known about the residency and properties of infiltrating monocytes after an inflammatory challenge. The meninges of the central nervous system (CNS) are populated by a dense network of macrophages that act as resident immune sentinels. Here we show that following lymphocytic choriomeningitis virus infection, resident meningeal macrophages (MMs) acquired viral antigen and interacted directly with infiltrating cytotoxic T lymphocytes, which led to macrophage depletion. Concurrently, the meninges were infiltrated by inflammatory monocytes that engrafted the meningeal niche and remained in situ for months after viral clearance. This engraftment led to interferon γ-dependent functional changes in the pool of MMs, including loss of bacterial and immunoregulatory sensors. Collectively, these data indicate that peripheral monocytes can engraft the meninges after an inflammatory challenge, imprinting the compartment with long-term defects in immune function.

Introduction

Macrophages are present in all tissues and participate in a plethora of different homeostatic functions, including iron metabolism in the liver, surfactant production in the lung, and synapse pruning in the central nervous system (CNS) parenchyma[1,2]. Recent studies have significantly advanced the field of macrophage biology by showing that most tissue-resident macrophages have an embryonic origin and receive varying degrees of input from the

Corresponding Author: Dorian B. McGavern, Ph.D. National Institutes of Health, Building 10, Room 5N240C, Bethesda, MD 20892, mcgavernd@mail.nih.gov, Phone: 301-443-7949.

Author contributions

R.R. conceived the project, designed, executed and interpreted the animal studies, analyzed data and wrote the manuscript; J.Y.L., A.B.S., I.S.S. executed animal studies and analyzed data. D.M. executed animal studies. K.R.J. analyzed data. D.B.M. conceived the project, designed and interpreted the animal studies and wrote the manuscript.

Competing Interests Statement

The authors declare no competing interests.

Ethics statement

This study was carried out in strict accordance with the recommendations in the Guide for the Care and Use of Laboratory Animals of the National Institutes of Health. The protocol was approved by the NINDS Animal Care and Use Committee (Protocol Number: 1295–17).

periphery after birth[3,4]. As long-lived tissue residents, macrophages play a critical role in microbial detection and eradication[1,2] and contribute to tissue repair following damage by cleaning up debris, shaping the microenvironment, and providing trophic support[5]. Indeed, macrophages are incredibly plastic cells that can transform to deal with diverse tissue challenges – both physiologic and pathophysiologic.

The CNS consists of the brain and spinal cord that transmit information throughout the body via peripheral nerves[6]. The CNS parenchyma contains highly specialized cells such as neurons, astrocytes, oligodendrocytes, and microglia that are critical for organismal function[7] and thus are housed behind the blood brain barrier (BBB) – a structure that regulates metabolic and cellular exchange with the periphery[8]. In addition to the BBB, the CNS is covered by an assembly of overlapping protective layers referred to as the meninges[9,10]. The outer most layer (dura mater) lies just beneath the skull bone, is highly innervated, and contains fenestrated vessels without tight junctions[9,10]. Beneath the dura resides the arachnoid mater, which has tight junctions and serves as an important CNS barrier. The inner layer of the meninges is referred to as the pia mater and lies atop the glial limitans. Together, these cellular layers surrounding the CNS parenchyma can support a considerable amount of immune traffic and are inhabited by specialized tissue-resident macrophages.

The CNS was once considered an immune privileged site devoid of immune cells, other than microglia, and without a classical lymphatic drainage system[11]. However, it is now generally accepted that the CNS is immunologically specialized and does support immune activity, albeit in highly regulated manner[12–14]. Most immune responses first develop outside the parenchyma in CNS barrier structures such as the perivascular spaces, choroid plexus, and meninges[12]. Despite the importance of the meninges to CNS immunity[9,10], little is known about the immune cell populations that inhabit this compartment under steady state and inflammatory conditions. The dura mater, for example, is inhabited by specialized tissue-resident macrophages that constantly survey their environment, similar to parenchymal microglia[15–17]. These macrophages are strategically located at the surface of the CNS alongside fenestrated blood vessels and thus have the potential to influence the underlying parenchyma during states of inflammation[10,12,18]. It is therefore important to understand how these cells are maintained and regulated.

Using lineage-tracing methods and macrophage markers (e.g. CX3CR1), it was recently discovered that, with exception of myeloid cells in the choroid plexus, macrophages residing in CNS barrier structures are derived from yolk-sac erythromyeloid precursors and are not replaced by blood monocytes during adulthood[4,16,19]. Monocytes do, however, contribute to the pool of choroid plexus macrophages over time. While these studies provide important insights into the homeostasis of CNS barrier macrophages, little is known about the origin, dynamics, and function of these macrophages during and after an inflammatory challenge. The meninges harbor one of the most abundant populations of barrier macrophages. Here, we comprehensively explored the dynamics of these cells before, during, and after an inflammatory viral challenge. We utilized genomic, intravital imaging, and cell tracking approaches in combination with novel assessments of macrophage function to define how infection reshapes the myeloid cell landscape within the meninges. Determining the

influence of cellular ontogeny and tissue microenvironment on resident macrophage functions is an area of crucial importance in the field[1,20]. Our study sheds light on how the specialized macrophage pool residing in the meninges can be fundamentally altered by an inflammatory challenge.

Results

Resident macrophages are distributed throughout the meninges

We first analyzed the distribution of MMs in meningeal whole mounts[21] obtained from naive mice. We identified MMs by staining for the mannose receptor, CD206, which was previously shown to label perivascular macrophages[22]. Under steady and inflammatory conditions, anti-CD206 staining labeled bona fide resident MMs that also expressed MerTK, CD64, TIMD4, and Lyve-1, but not CD11c (Supplementary Fig. 1a–c). MMs were found adjacent to blood vessels throughout the dura mater and were also found in the central and lateral sutures (Fig. 1a). Two-photon imaging of naive mice expressing the green fluorescent protein (GFP) under the *Cx3cr1* promoter (*Cx3cr1*$^{gfp/+}$ mice) through a thinned skull window[23] revealed that MMs have very active processes, and constantly surveyed their surroundings similar to microglia (Fig. 1b; Supplementary Videos 1,2). We also observed by flow cytometry that naive MMs express common macrophage markers (CD11b, F4/80, CD64) as well as costimulatory (CD80), antigen-presenting (MHC I, MHC II), and adhesion molecules (ICAM) (Fig. 1c). Collectively, these data suggest that MMs play an important role as innate sentinels in the lining of the CNS.

MMs are infected and activated during viral meningitis

To address the role of MMs in response to an inflammatory challenge, we infected mice with lymphocytic choriomeningitis virus (LCMV). Intracranial injection of LCMV triggers meningeal inflammation characterized by infiltration of virus-specific $CD8^+$ T cells and myelomonocytic cells[24,25]. This infection model results in edema, brain herniation, and death within 6 days[26]. We observed 4 days following LCMV infection that approximately one-third of MMs were infected by the virus (Fig. 2a,b) and that antiviral cytokines (interferon-β (IFN-β), IFN-γ and tumor necrosis factor, TNF) were upregulated within the meninges as early as day 2 post-infection (Fig. 2c). To determine how MMs responded to this environment, we performed a microarray on sorted MMs from mice infected 4 days prior with LCMV and compared them to MMs from mock-infected mice. In response to infection, the MM transcriptome was markedly changed, with 39 down- and 176 up-regulated genes (Supplementary Table 1). Upregulation of several different activation markers (MHC I, CD54, CD36, CD80, CD274, SR-A, CCR5) was also confirmed at the protein level (Supplementary Fig. 2a,b). Ingenuity pathway analysis revealed that most of these differentially regulated genes were downstream of the cytokines (IFN-β, IFN-γ, TNF) that were upregulated in the meninges (Fig. 2c **and** Supplementary Table 1**)**. Consistent with this pattern, the MMs from infected mice showed evidence of interferon- and mitogen-activated protein kinase (MAPK)-signaling (Fig. 2d) as well as upregulation of genes associated with important immune functions, such as phagocytosis, endocytosis, antigen presenting cell activity, and antiviral activity (Fig. 2e). These data indicate that MMs are

highly responsive to a LCMV challenge, can uptake viral antigen and profoundly change their activation status.

MMs are killed during viral meningitis

We next examined the fate of MMs during viral meningitis. Death receptor and apoptosis signaling were among the pathways detected in MMs by microarray analysis at day 4 post-infection, suggesting that these cells were undergoing programmed cell death. Consistent with this hypothesis, the density of $CD206^+$ MMs decreased significantly by day 6 post-infection (Fig. 3a; Supplementary Fig. 3a–c). This decrease was not due to CD206 downregulation, as the number of MMs identified by TimD4 and Lyve1 staining was similarly decreased following infection (Supplementary Fig. 3d,e). This finding coincided with frequent engagements of *Cx3cr1*$^{gfp/+}$ cells by LCMV-specific cytotoxic lymphocytes revealed by two-photon microscopy (Fig. 3b; Supplementary Video 3). We also assessed the extent of MM cell death by injecting mice intravenously at the peak of the disease with propidium iodide (PI) - a cell membrane impermeable DNA dye. This approach combined with histocytometric analysis revealed that ~26% of remaining *Cx3cr1*$^{gfp/+}$ cells at day 6 post-infection were PI^+ (Fig. 3c,d) and that dead cells localized predominantly along central suture of the meninges (Fig. 3e). These data indicate that many MMs are killed during LCMV meningitis.

Infected MMs are cleared and replaced after meningitis

To understand how the myeloid niche was replaced after meningitis, we used an attenuated recombinant of LCMV that expresses three RNA segments (r3LCMV)[27,28]. Whereas wild-type bi-segmented LCMV induces fatal disease in all mice at day 6, infection with r3LCMV resulted in sub-lethal meningitis (Fig. 4a). Viral RNA was detected in the meninges at day 6 post-infection, but dropped to background levels at days 15 and 30 post-infection, indicating viral clearance (Fig. 4b). In this model, MMs were also killed after the first week of infection (Supplementary Fig. 4a–c). Interestingly, the MM niche at day 30 was completely replenished, and the number and dynamics of these cells were indistinguishable from mock-infected control mice (Fig. 4c and Supplementary Video 4). As tissue-resident CNS macrophages have a long lifespan[16], we next addressed whether previously infected MMs survived until day 30. This analysis was accomplished by conducting a fate-mapping study in which we infected floxed Stop TdTomato reporter (Stop$^{fl/fl}$ TdTomato) mice with r3LCMV-iCre[28]. This system allows permanent fluorescent protein labeling of infected cells and their progeny even after the virus is cleared. Four days following r3LCMV-iCre infection, more than a third of MMs were infected and became TdTomato-positive (Fig. 4d–f). Most of these infected cells disappeared by day 30 post-infection, with only 5% of the MM pool remaining TdTomato-positive (Fig. 4d–f). Of note, most $CD206^-CD45^-$ stromal cells infected at day 6 by r3LCMV-iCre were still present at day 30, indicating that not all infected cell populations in the meninges are cleared in a cytopathic manner (Fig. 4e,f). Analysis of meningeal whole mounts confirmed that most of the TdTomato-positive signal at day 30 (indicative of previously infected cells) was negative for CD206 (Fig. 4f). These data demonstrate that following infection, infected MMs were eliminated, and that the meningeal niche was replenished within a month.

Viral infection induces long-term engraftment by peripheral monocytes

Wild-type LCMV and r3LCMV infection promoted robust monocyte recruitment into the meninges at days 4 and 6 (Supplementary Fig. 4d,e); however, repopulation of the MM niche following viral clearance could occur by local proliferation of myeloid precursors and/or engraftment by peripheral blood monocytes. To distinguish between these two possibilities, we first generated chimeras by irradiating head-shielded C57BL/6 mice and reconstituting with bone marrow from actin-teal fluorescent protein (TFP) mice[29]. These chimeric mice were then infected with r3LCMV, and thirty days later, we observed increased engraftment of the $CD206^+$ MM compartment by bone marrow-derived TFP^+ cells in virally infected mice relative to mock (PBS)-infected controls (Supplementary Fig. 5a,b). This engraftment occurred without a change in overall MM cell numbers between the two groups (Supplementary Fig. 5c). To further confirm the meningeal engraftment of peripheral cells, we conducted a lineage-tracing experiment[3,30]. Briefly, *Cx3cr1*$^{CreER/+}$ × $Stop^{fl/fl}$ TdTomato mice were pulsed with tamoxifen for a week. This treatment efficiently labelled nearly all MMs (Supplementary Fig. 5d,e). Forty days later, mice were inoculated with r3LCMV or PBS (Fig. 5a). Approximately 77.8 ± 3.1% (mean±SEM) of $CD206^+$ MMs were TdTomato-positive in mock-infected mice at day 30, indicating a relatively low turnover of resident myeloid cells over 70 days. By contrast, 48.0 ± 3.8% (mean±SEM) of $CD206^+$ MMs were TdTomato-negative in day 30 r3LCMV-infected mice (Fig. 5a, **left**), suggesting engraftment by peripheral blood monocytes. A similar degree of engraftment was observed at 2 and 6 months post-infection (Supplementary Fig. 5f,g). As additional controls for this experiment, we confirmed that nearly all brain-resident microglia were comparably TdTomato-positive in mock- and r3LCMV-infected mice (Fig. 5a, **middle**), whereas nearly all blood-derived myeloid cells were TdTomato-negative (Fig. 5a, **right**). To determine the anatomical distribution of engrafting TdTomato-negative monocytes after LCMV infection, we performed histocytometry on meningeal whole mounts from day 30 r3LCMV- versus mock-infected mice. We confirmed that TdTomato-negative myeloid cells were more abundant in LCMV-infected mice and localized throughout the meninges (Fig. 5b,c), which is consistent with the hypothesis that LCMV induces extravasation of monocytes from meningeal blood vessels that differentiate locally into $CD206^+$ macrophages.

IFNγ promotes differentiation of engrafting monocytes.

We next assessed the inflammatory profile of the mixed chimeric MM population following resolution of an LCMV infection. Relative to mock-infected controls, we observed that MHC I expression was elevated on MMs from r3LCMV-infected mice at day 30 (Fig. 6a,b). A similar increase was observed in MHC II expression following infection, which resulted in an increased proportion of MHC II^+ MMs in r3LCMV-infected mice (Fig. 6c,d). Interestingly, lineage tracing studies at day 30 post-infection revealed that blood-derived TdTomato-negative myeloid cells accounted for the elevated proportion of MHC II^+ cells (Fig. 6e). This finding led us to investigate the genomic signature of the engrafted MHC II^+ meningeal myeloid cells and the mechanism that gave rise to this phenotype following r3LCMV infection. Using the gating strategy shown in Supplementary Fig. 6a, we performed a microarray on sorted MHC II^+ MMs from day 30 mock- versus r3LCMV-infected mice and compared the expression profiles to those of MHC II^- cells. In both

groups, more than 270 genes were differentially expressed by the two MM populations, and IFN-γ was the main upstream regulator of the MHC II$^+$ MM population, regardless of the infection status (Fig. 6f,g; Supplementary Table 2). Because IFN-γ was produced in the meninges early after LCMV infection, we theorized that this antiviral cytokine might shape the myeloid cell engraftment program. To specifically assess whether IFN-γ signaling on myeloid cells was responsible for this phenotype, we generated *LysM*$^{Cre/+}$ × *Ifngr1*$^{fl/fl}$ mice, in which these cells are unable to sense IFN-γ. Using adult *LysM*-GFP mice, we confirmed that this promoter is active in MMs and monocytes, but not microglia (Supplementary Fig. 6b–e). In *LysM*$^{Cre/+}$ x *Ifngr1*$^{fl/fl}$ mice, IFN-γR protein expression was reduced by >50% on MMs and circulating monocytes (Supplementary Fig. 7a–d), which did not alter the number or profile of MMs during steady state or following PBS injection (Supplementary Fig. 8a–c). However, at day 30 post-r3LCMV infection, we revealed that the frequency of MHC II$^+$ MMs as well as the expression of MHC I on these cells was reduced in infected *LysM*$^{Cre/+}$ × *Ifngr1*$^{fl/fl}$ mice relative to wild-type control mice (Fig. 6h,i). This result was not associated with a reduction in the absolute number of MMs (Supplementary Fig. 8d). These data collectively indicate that IFN-γ is at least one of the cytokines required to differentiate infiltrating monocytes that engraft the depleted MM niche following LCMV infection.

Infection alters the MM microbial ‘sensome’

Our microarray analyses of sorted MHC II$^+$ vs MHC II$^-$ MMs from mock- and r3LCMV-infected mice at day 30 revealed that LCMV infection triggers differential expression of 74 genes (34 up; 40 down) in MHC II$^+$ cells and 39 genes (13 up; 26 down) in MHC II$^-$ cells (Supplementary Table 3; Supplementary Fig. 9a–b). Interestingly, almost no overlap was observed between the differentially expressed genes induced by LCMV at the peak of viral disease (day 4) (Supplementary Table 1) relative to day 30 (Supplementary Table 3), suggesting that the changes observed in MMs at day 30 reflect reprogramming rather than the resolution of an inflammatory process. We therefore became interested in some of the specific MM changes following LCMV infection that might affect the future responsiveness of this compartment. For example, r3LCMV infection promoted a significant long-term reduction in a family of microbial sensors (CD209a,b,c,d,e,f) in both MHC II$^+$ and MHC II$^-$ MMs at day 30 (Supplementary Table 3). This family is closely related to human dendritic cell-specific intercellular adhesion molecule-3-grabbing non-integrin (DC-SIGN)[31]. Moreover, CD209b/SIGNR-1 is a C-type lectin receptor involved in recognition of microbial carbohydrates and down-stream inflammatory signaling[32–37]. We therefore analyzed SIGN-R1 expression on CD206$^+$ MMs by flow cytometry at day 30 (Fig. 7a,b). In mock-infected mice, ~20% of the MMs expressed SIGN-R1, and this percentage was markedly reduced in mice previously infected with r3LCMV (Fig. 7a,b). This observation was confirmed by histocytometry, which revealed a significant reduction in the percentage of SIGN-R1$^+$ MMs within meningeal whole mounts from r3LCMV-infected mice at day 30 (Fig. 7c,d). Interestingly, SIGN-R1 was expressed exclusively by MMs within the meninges and no other cell types, thus the reduction in expression following r3LCMV infection has the potential to influence microbial sensing (Fig. 7c). Moreover, using our lineage-tracing paradigm, we observed after infection that SIGN-R1 was found exclusively on resident TdTom$^+$ MMs, not engrafting TdTom$^-$ cells (Supplementary Fig. 10a,b). These data further support our conclusion that engrafting myeloid cells are the ones that give rise to an overall

phenotypic change in the MM niche. To test whether r3LCMV-infected mice had a reduced ability to respond to a microbial challenge at day 30, we challenged mice with lipopolysaccharide (LPS) as a surrogate for bacterial infection. Neutrophils were barely detectable in the meninges of r3LCMV memory or control mice (182 ± 46 versus 173 ± 56 neutrophils, respectively) prior to LPS challenge. After LPS challenge, r3LCMV-infected mice showed a defect in their ability to recruit neutrophils into the meninges (Fig. 7e). A similar reduction in neutrophil recruitment was observed following administration of a SIGN-R1 blocking antibody to uninfected mice that were subsequently challenged with LPS (Supplementary Fig. 10c,d). Collectively, these data demonstrate that day 30 r3LCMV-infected mice are indeed deficient in their ability to sense and respond to a secondary microbial challenge.

Infection alters anti-inflammatory MMs responses

In addition to microbial sensing, another important component of tissue-resident macrophage function is immune regulation. We observed based on our microarray analyses that the gene encoding a subunit of the nicotinic cholinergic receptor (*Chnrb4*) was down-regulated in MHC II^+ MMs from r3LCMV-infected mice relative to mock-infected controls at day 30 (Supplementary Table 2). This finding was confirmed by Q-PCR, which revealed a specific reduction in *Chnrb4* expression within sorted MHC II^+ (but not MHC II^-) MMs from day 30 infected mice (Fig. 8a). Acetylcholine was previously shown to dampen inflammatory reactions in peripheral macrophages[38]. We therefore tested whether MMs from r3LCMV-infected mice would fail to quench inflammation via acetylcholine. To deliver acetylcholine to MMs, we developed a novel approach that involved injecting an acetylcholine-containing hydrogel under the mouse scalp. We demonstrated previously that the skull bone is permeable to small molecules[18], and our hydrogel approach allowed acetylcholine to be delivered transcranially into the meninges.

To establish the effectiveness of this approach, we challenged naive mice with LPS in the presence or absence of acetylcholine loaded hydrogel and quantified expression of interferon-stimulated gene 15 (*Isg15*) in the meninges as a surrogate for the induction of an inflammatory response (Fig. 8b). This experiment revealed that pre-incubation with the acetylcholine hydrogel efficiently dampened *Isg15* induction (Fig. 8b). We also confirmed that sorted MMs respond to LPS *in vivo* by upregulating *Isg15* (Fig. 8c). MMs were a predominate source of *Isg15* expression. Having established this assay, we finally assessed the potential of MMs from mock- vs. r3LCMV-infected mice to dampen *Isg15* expression in presence of acetylcholine. MMs from both groups at day 30 responded comparably to LPS challenge by upregulating *Isg15* expression (Fig. 8d); however, r3LCMV-infected mice showed a reduced ability to quench this response in the presence of acetylcholine (Fig. 8e), which is consistent with the decreased expression of acetylcholine receptors in MMs (Fig. 8a). These data indicate that MMs from previously infected mice have a reduced ability to dampen inflammation due to alterations in cholinergic receptor expression.

Discussion

Tissue resident macrophages are typically long-lived cells that participate in tissue homeostasis, repair, and the defense against invading pathogens. Within the CNS, microglia represent the most well-described tissue resident macrophage population. Here, we demonstrate that the dura mater of the meninges is also inhabited by a dense network of highly dynamic resident macrophages. LCMV infection of the meninges triggers a well-described meningitis[26], resulting in robust innate and adaptive peripheral immune cell invasion that leads to significant depletion of MMs. By developing a model to study the recovery from viral meningitis, we discovered that viral clearance coincides with engraftment by inflammatory monocytes that differentiate in an IFNγ-dependent manner into resident MMs with altered phenotypic and functional properties. This engraftment persists for months and skews the properties of the MM landscape, impeding its ability to detect microbes and respond to immunoregulatory signals like acetylcholine. These data indicate that viral infection can imprint an important CNS barrier macrophage system with new properties that alters its response to subsequent challenges.

Much like barrier surfaces in the intestines, lung, skin and liver[1], we found that the dura mater, a CNS barrier surface, is inhabited by a dense network of MMs. Under steady state conditions, we observed that MMs express antigen-presenting (MHC I, MHC II), adhesion (ICAM-1), scavenging (CD64), and costimulatory (CD80) molecules and high levels of CD206 – a marker commonly expressed by alternatively activated macrophages[39,40] and other CNS barrier macrophages[41,42]. It is likely that meningeal macrophages are maintained in an anti-inflammatory state to help maintain CNS homeostasis and neurological function[43,44]. Following viral infection of the meninges, we found that MMs were rapidly activated and acquired antigen, triggering engagement by infiltrating cytotoxic lymphocytes (CTL). Using a fluorescent protein reporter system to track the fate of LCMV-infected cells and their progeny, we observed that infected MMs disappeared during the inflammatory process associated with viral clearance.

Under steady state conditions, the origin and turnover of tissue resident macrophages varies among tissues[3,4]. Our study indicates that dural macrophages received monocytic input during steady state (similar to choroid plexus macrophages)[16], which is likely due to the higher permeability of dural blood vessels relative to most other CNS blood vessels. During inflammation, blood monocytes can invade tissues and their fate (death or engraftment) is just starting to be elucidated[45]. Our data demonstrate that peripheral myeloid cell engraftment in the dura mater was enhanced by virus-induced inflammation. Rapid and efficient recruitment of blood monocytes was followed by IFNγ-dependent differentiation into MHC II^+ macrophages and long-term meningeal engraftment. The generation of inflammatory cytokines after viral infection likely favors peripheral immune cell engraftment versus proliferation of residents. A better understanding of the factors that promote local proliferation versus peripheral myeloid cell engraftment may someday give rise to drugs that can influence macrophage repopulation of tissues following inflammation.

Another question raised by the recent discoveries of tissue resident macrophage origins relates to the link between ontogeny and function. During homeostasis, macrophage

functions are principally driven by the tissue microenvironment rather than cellular origin[45–48]. However, acute inflammation promotes recruitment of monocyte-derived macrophages that can either phenocopy the resident macrophage pool or dramatically change the immune properties of the tissue[49–51]. Knowing the functional properties of engrafting monocytes is crucial when considering how that tissue will respond to future inflammatory challenges. In our study, we revealed following the resolution of meningeal inflammation that engrafting monocyte-derived macrophages showed differences in genes related to their 'sensome' when compared with the resident macrophage pool. A notable example was the reduction in CD209b (aka SIGN-R1). SIGN-R1, the mouse homolog of human DC-SIGN, is a C-type lectin receptor that mediates the immune recognition of bacterial motifs (e.g. lipopolysaccharides)[31,36,37]. Engraftment of the MM pool by monocytes resulted in a sizeable loss in the anatomical distribution of available SIGN-R1 within the dura mater (Fig. 7c), and we propose that this loss contributed to the reduced recruitment of neutrophils into the meninges following LPS challenge. A defect in macrophage pathogen sensing following meningeal inflammation could render this compartment susceptible to future infections and/or contribute to recurrent meningitis[52]. Our results also provide new insights into the concept of innate memory which is usually associated with epigenetic changes that can either result in enhancement (trained immunity) or impairment (tolerance)[53]. We propose that changes occurring at the population level, such as engraftment by functionally distinct macrophages, could also contribute to innate memory following the resolution of inflammation.

Another functional defect we observed in the engrafting pool of MMs was their reduced ability to dampen an inflammatory signal (ISG15) in response to acetylcholine. Acetylcholine derived from $CD4^+$ T cells or vagal nerves can quench inflammatory reactions in macrophages[54]. The dura mater is innervated by parasympathetic branches of the trigeminal ganglion that produce acetylcholine[9]. We observed that expression of the nicotinic cholinergic receptor was markedly reduced on the MHC II^+ subset of engrafting macrophages, which impeded their ability to dampen LPS-induced ISG15 following transcranial administration of acetylcholine. A loss of neuro-immune crosstalk and immunoregulatory functions in the meninges following meningitis could predispose the CNS to subsequent inflammation.

In conclusion, our studies shed light on how a viral infection can imprint the myeloid cell landscape at the brain surface, giving rise to long term functional changes. Following meningitis, engraftment by peripheral macrophages opens potential susceptibilities in this dural defense system that render it less able to sense microbes and regulate immunity. The meninges represent the first layer of defense against microbial challenges and serves as a gateway for immune cell traffic into the CNS[9,10]. Thus, the replacement of tissue resident dural macrophages by inflammatory monocytes has the potential to profoundly influence CNS immunity, homeostasis, and neurological function.

Accession codes

The files of the microarray study have been deposited in the NCBI GEO database and are available for download (accession no. GSE108648).

Methods

Mice.

C57BL/6J (B6), B6.129S7-*Ifn*^{tm1Ts}/J (*Ifng*$^{-/-}$), B6.129P-Cx3cr1tm1Litt/J (*Cx3cr1*$^{gfp/gfp}$), B6.129P2(Cg)-Cx3cr1tm2.1(cre/ERT2)Litt/WganJ (*Cx3cr1*$^{CreER/CreER}$), C57BL/6N-Ifngr1tm1.1Rds/J (*Ifngr1*$^{fl/fl}$), B6.129P2-Lyz2tm1(cre)Ifo/J (*LysM*$^{Cre/Cre}$), B6.Cg-Gt(ROSA)26Sortm14(CAG-tdTomato)Hze/J (Stop$^{fl/fl}$ TdTomato) were purchased from The Jackson Laboratory. *Cx3cr1*$^{gfp/gfp}$, *Ifngr1*$^{fl/fl}$, *LysM*$^{Cre/Cre}$, Rosa26iDTR, and Stop$^{fl/fl}$ TdTomato were then bred and maintained under specific pathogen free conditions at the National Institute of Health (NIH). B6 D^{b}GP$_{33–41}$ TCR-tg (P14), actin-TFP[29] and actin-OFP[29] were also bred and maintained at the NIH. *Cx3cr1*$^{CreER/+}$ Stop$^{fl/fl}$ TdTomato, *Cx3cr1*$^{gfp/+}$ and OFP^{+} P14 were derived from the following F1 crosses: *Cx3cr1*$^{CreER/CreER}$ × Stop$^{fl/fl}$ TdTomato mice, B6 × *Cx3cr1*$^{gfp/gfp}$ mice and actin-OFP × P14. *LysM*$^{Cre/+}$ *Ifngr1*$^{fl/fl}$ mice were obtained in the F2 generation by originally crossing *LysM*$^{Cre/Cre}$ and *Ifngr1*$^{fl/fl}$ mice. Male and female mice in this study were used at 6–8 weeks of age. All mice in this study were handled in accordance with the guidelines set forth by the NIH Animal Care and Use Committee and the recommendations in the AAALAC Guide for the Care and Use of Laboratory Animals. The protocol was approved by the NINDS Animal Care and Use Committee.

Virus.

To induce meningitis and subacute meningitis, adult mice at 6 to 8 weeks of age were infected intracerebrally (i.c.) with 1×10^3 plaque forming units (PFU) of LCMV Armstrong clone 53b, 1.5×10^4 PFU r3LCMV-iCre[28], or 1.5×10^4 PFU r3LCMV-TFP[24]. Survival following infection was monitored daily. Stocks were prepared by a single passage on BHK-21 cells, and viral titers were determined by plaque formation on Vero cells.

Generation of r3LCMV.

Virus rescue of r3LCMV-iCre and r3LCMV-TFP was performed as described previously[27].

Tamoxifen treatment.

For induction of Cre recombinase, 6- to 8-week-old *Cx3cr1*$^{CreER/+}$ Stop$^{fl/fl}$ TdTomato mice received daily intraperitoneal injections (for 5 days) of 2 mg tamoxifen (TAM, Sigma-Aldrich) dissolved in 100 μl corn oil (Sigma).

In vivo cell death assay.

Mice were injected with 100 μg propidium iodide in water (PI; Invitrogen) i.v. for 1 h. Mice were anesthetized, perfused, and meningeal tissue was processed as described below.

Meningeal whole-mount immunohistochemistry.

Mice were anesthetized with chloral hydrate and perfused with 5% neutral buffered formalin (NBF) for *in vivo* cell death assays involving propidium iodide or with phosphate buffered saline (PBS) for subsequent antibody staining. Skull caps were removed, and following a brief wash in PBS, meninges were incubated at room temperature (23°C) for 15 min in 1.5

ml of blocking solution containing mouse IgG (0.5 mg/ml, Jackson Research) and Fc Block CD16/32 (5 μg/ml, BioLegend). The meninges were subsequently stained with primary antibodies at room temperature (23°C) for 1 h. The following primary antibodies were used: Alexa488 and Alexa647 anti-CD206 (2.5 μg/ml; clone C068C2; BioLegend), APC anti-SIGN-R1 (2.5 μg/ml; clone 22D1; eBioscience), Pacific Blue and Alexa647 anti-IA^b/IE^b (1.25 μg/ml; clone M5/114.15.2; BioLegend), Pacific Blue and PE anti-CD31 (1.25 μg/ml; clone 390; BioLegend). All antibodies were placed in 1.5 ml of PBS + 2% fetal bovine serum (staining buffer). Meninges were then washed three times in staining buffer for 30 s and fixed overnight at 4 °C in 5% NBF. The following day the meninges were carefully removed from the skull caps with fine-tipped forceps. The meninges were placed in mounting medium (FluorSave Reagent with or without DAPI; Vectashield) on a glass slide, spread out and flattened with forceps, and cover-slipped. Fluorescent images were acquired using an Olympus FV1200 laser scanning confocal microscope equipped with 405, 458, 488, 515, 559, and 635 laser lines, 4 side window PMTs for simultaneous 4 channel acquisition, and 4×/0.16, 10×/0.4, 20×/0.75, 40×/0.95, and chromatic aberration corrected 60×/1.4 NA objectives. 3D tile scans encompassing the entire meninges were collected (*z* depth = 400 μm, *z* step size = 20 μm) and analyzed using Imaris 8.1.2 software.

Histocytometry.

After collecting tile scans by confocal microscopy, entire meningeal whole mounts or specific anatomical regions within the meninges (e.g. lobe, suture) were analyzed by histocytometry. The Surface Creation Wizard in Imaris 8.1.2 software was used to threshold on and identify positively stained cells within the 3D meningeal tile scans. Once identified a value-based visual surface was generated for all positively stained cells, which enabled quantification of fluorescence intensity as well as the frequency of labeled and unlabeled cells. Channel statistics for TdTomato, propidium iodide, or SIGN-R1 signal were obtained for 3D cellular surfaces defined based on CD206 or CX3CR1. These channel statistics were subsequently exported into Excel (Microsoft), and mean voxel fluorescence was plotted in FlowJo software by utilizing the Text to FCS conversion utility (TreeStar Inc). Percentages of surfaces either positive or negative for TdTomato, propidium iodide, or SIGN-R1 were gated using traditional log-scale based flow cytometry plots in FlowJo and then graphed on linear *xy* plots to map their respective positions within the meninges. This approach was also used to quantify cell densities labeled and unlabeled cells within the meninges.

Mononuclear cell isolation.

Anesthetized mice received an intracardiac perfusion with PBS to remove contaminating erythrocytes. Leukocytes were isolated from the meninges using forceps to gently separate them from the underside of skull cap (the same method used to prepare meningeal whole mounts above). This was followed by enzymatic digestion in RPMI containing 2.5 mg/ml collagenase D (Roche) + 0.1 mg/ml DNase (Roche) for 30 min at 37 °C with gentle shaking every 10 min. Leukocytes were isolated from the brain as described[55]. Following digestion, supernatants were isolated, washed, and finally passed through a 35-μm pore cell strainer. After this step, meningeal cells were used for staining. Cells from the brain, however, were resuspended in a 90/60/40% discontinuous Percoll (GE Healthcare) gradient in HBSS and

centrifuged to remove myelin and debris from the preparation. Afterwards, brain leukocytes were then stained comparably to meningeal cells.

Blood processing.

Blood samples were collected by retro-orbital bleeding using capillary tubes and placed in EDTA-tubes (Sarstedt). Red blood cells were lysed as described[55] and samples were washed twice with PBS containing 2% FBS before antibody staining.

Flow cytometry.

Surface staining was performed by incubating cell suspensions for 20 min on ice with cocktails of mAbs in PBS containing 2% FBS. Prior to staining, cell preparations were blocked with 5 μg/ml rat anti–mouse CD16/32 (Fc receptor block; BD) and 0.5 mg/ml whole mouse IgG (Jackson ImmunoResearch Laboratories, Inc.) for 10 min on ice to reduce unspecific antibody binding. Dead cells were excluded from the analysis by using the LiveDead fixable Blue Cell Staining kit (Invitrogen) or 7-AAD stain (BioLegend). The following antibodies were obtained from BioLegend (BL), BD, or eBioscience (eB): CD45 Brilliant Violet 650 (104, BL), CD11b Brilliant Violet 605 (M1/70, BL), CD90.2 (Thy1.2) Brilliant Violet 785 (30-H12, BL), Ly6G Brilliant Violet 711 (RA3–6B2, BL), F4/80 Brilliant Violet 510 (BM8, BL), CD206 PerCP/Cy7 (C068C2, BL), IA^b/IE^b Pacific Blue (M5/114.15.2, BL), H-$2D^b$ H-$2K^b$ FITC (28–8-6, BL), Ly6C PerCP/Cy5.5 (HK1.4, eB), CD8β.2 PE (53–5.8, BL), Gr1 Alexa647 BD (RB6–8C5) , SIGN-R1 APC (eB), CD80 PE (16–10A1, BL), ICAM Alexa 488 (YN/7.7.4, BL), CD64 Alexa 647 (X54–5/7.1, BL), MERTK PE-Cyanine7 (DS5MMER, eB), CD11c PE-Cyanine7 (N418, BL), CD54 APC (YN1/1.7.4, BL), CD36 Alexa488 (HM36, BL), CD274 biotin (10F.962, BL), IFN-γR biotin (RDI-MCD119-GRBT, Fitzgerald), Streptavidin 647 (BL), SR-A (MRS1, BL), CCR5 Alexa647 (HM-CCR5, BL), TimD4 Alexa647 (RMT4–54, BL), Lyve-1 Alexa488 (ALY7, eB) and corresponding isotype controls. For intracellular staining to detect LCMV, single-cell suspensions were first stained with surface antibodies and were then treated with Cytofix/Cytoperm (BD). This was followed by intracellular staining anti–mouse LCMV (VL-4; Bio X Cell). Anti-LCMV mAb was directly conjugated to Alexa Fluor 647 using an antibody-labeling kit from Invitrogen. Samples were acquired using an LSRII digital flow cytometer (BD), and data were analyzed using FlowJo software version 9.7.2 (Tree Star).

Adoptive transfers.

Mice were seeded i.v. with 10^5 OFP^+ P14 $CD8^+$ T cells in PBS purified from the splenocytes of naive transgenic mice using a CD8 negative selection kit (Stem Cell Technologies). The purity after enrichment was determined to be greater than 98%. One day later the mice were challenged i.c. with LCMV Armstrong.

Bone marrow (BM) chimeras.

BM was harvested from femurs and tibias of actin-TFP mice and 10^7 BM cells were i.v. injected into recipient mice following a lethal irradiation dose of 950 RAD. The head was shielded with lead to avoid exposing the brain and meninges to radiation. Mice received

antibiotics in drinking water for 4 weeks following irradiation and were allowed 6 weeks to reconstitute their hematopoietic system.

In vivo cell depletions.

Mice were depleted of $CD8^+$ T cells by i.v. injection 200 μg anti-CD8 (clone YTS 169.4; BioXcell) on day 0 and 4 post-infection.

Acetylcholine administration.

Acetycholine-containing hydrogel was made by dissolving acetylcholine (Sigma) in 4 ml of PBS, at a concentration of 20 mg/ml, and then adding carboxymethycellulose (10 mg/ml, Sigma) in a Becher under agitation. Five minutes later, 300 μl of hydrogel were then injected subcutaneously under the scalp of adult mice. Mock-hydrogel was prepared in parallel, in the same way, without acetylcholine.

LPS injections.

LPS (Sigma) was dissolved in PBS at a concentration of 0.1 mg/ml, and 30 μl were injected intracerebrally. In other experiments, LPS was injected intraperitoneally at a dose of 0.4 mg/kg.

Two-photon microscopy.

Mice were anesthetized, and thinned skull windows were prepared as previously described[55,56]. Mice were injected with 50 μg Evans blue where indicated to visualize blood vessels. 4D datasets were acquired using a Leica SP8 two-photon microscope equipped with an 8,000-Hz resonant scanner, a 25× color corrected water-dipping objective (1.0 NA), a quad HyD external detector array, a Mai Tai HP DeepSee Laser (Spectra-Physics) tuned to 905nm (for GFP, Alexa Fluor 488, Evans blue, propidium iodide) and an Insight DS laser (Spectra-Physics) tuned to 1050 nm (for red-fluorescent protein). 3D time-lapse movies were captured in *z*-stacks of 10–30 planes (2 μm step size) at 40 sec intervals. Signal contrast was enhanced by averaging 10–12 video frames per plane in resonance scanning mode.

Isolation of $CD206^+$ macrophages.

$CD206^+$ macrophages were isolated from PBS or LCMV-infected mice at day 4 and day 30 post-infection using a FACS Aria Digital Cell Sorter (BD) and MoFlo Astrios EQ from Beckman Coulter equipped with an integrated BSL-2 enclosure. Meningeal cells were extracted and stained as described in the Mononuclear cell isolation and Flow cytometry sections above. Depending on the experiment, four different cell populations ($CD206^+$ macrophages, $CD206^+$ $MHCII^+$ macrophages, $CD206^+$ $MHCII^-$ macrophages and/or $F4/80^{neg}$cells) were sorted to >95% purity.

Microarray analysis.

For day 4 microarray analyses, total RNA of $CD206^+$ macrophages isolated from PBS or LCMV-infected mice (four independent experiments with ninety mice per group) was labeled on a sample-by-sample basis according to the manufacturer's guidelines for use with

the MoGene-2_0-st GeneChip (Affymetrix). Labeled cRNA were hybridized to these arrays in blinded interleaved fashion. The Scanner 3000 (Affymetrix) was used in conjunction with Affymetrix's AGCC software (v4.0) (Affymetrix) to generate one .CEL file per hybridized cRNA. These files have been deposited in the NCBI GEO database and are available for download (accession no. GSE108648). The Expression Console (Affymetrix) was next used to summarize the data contained across all .CEL files and generate 41,345 RMA normalized gene probe expression values per file. Quality of this expression was challenged and assured via Tukey box plot, covariance-based PCA scatter plot, and correlation-based heat map using functions supported in "R" (http://www.cran.r-project.org). To remove noise-biased expression values, Lowess modeling was performed using expression values by class (CV~mean expression). Lowess fits were then over-plotted to identify the common low-end expression value where the relationship between mean expression (signal) and CV (noise) deviated from linearity (mean expression value = 3.75). Afterwards, expression values were floored to equal this value if less while expression for probes not greater than this value for at least one sample were discarded as non-informative. Expression values for remaining probes were then tested between treatment conditions (LCMV vs PBS) using the Welch-modified *t*-test under Benjamini–Hochberg (BH) false discovery rate (FDR) multiple comparison correction conditions. Probes with a corrected $P < 0.05$ by this test and a linear magnitude difference of means ≥ 1.5× between treatment conditions were considered significantly and robustly dysregulated between LCMV and PBS treatment. Annotations for the dysregulated probes identified were obtained from NetAffx (Affymetrix). The corresponding enriched pathways and functions for the dysregulated probes were identified using IPA (Ingenuity). For the day 30 microarray analyses, total RNA of $CD206^+$ MHC II^+ and $CD206^+$ $MHCII^-$ macrophages isolated from PBS or LCMV-infected mice (four independent experiments with ninety mice per group) was labeled on a sample-by-sample basis according to the manufacturer's guidelines for use with the Mouse Clariom S GeneChip (Affymetrix). Labeled cRNA were hybridized to these arrays in blinded interleaved fashion. The Scanner 3000 (Affymetrix) was used in conjunction with Affymetrix's AGCC software (v4.0) (Affymetrix) to generate one CEL file per hybridized cRNA. These files have been deposited in the NCBI GEO database and are available for download (accession no. GSE108648). The Expression Console (Affymetrix) was next used to summarize the data contained across all CEL files and generate 22,206 SST-RMA normalized transcript cluster expression values. Quality of this expression was challenged and assured via Tukey box plot, covariance-based PCA scatter plot, and correlation-based heat map using functions supported in "R" (http://www.cran.r-project.org). To remove noise-biased expression values, Lowess modeling was performed using expression values by class (CV~mean expression). Lowess fits were then over-plotted to identify the common low-end expression value where the relationship between mean expression (signal) and CV (noise) deviated from linearity (mean expression value = 3.75). Expression values for transcript clusters across samples were floored to equal this value if less while expression for transcript clusters not greater than this value for at least one sample were discarded as non-informative. For transcript clusters not discarded, ANOVA testing of the expression values across samples using class as the factor was performed under BH FDR multiple comparison condition. Transcript clusters observed to have a corrected $P < 0.05$ by this test were then post hoc challenged via TukeyHSD test. Transcript clusters observed to have a post hoc P <

0.05 and an absolute difference of means ≥ 1.5× for a class comparison were then subset for that comparison as having differential expression between the two classes respectively. Annotations for these subset transcript clusters were next obtained from NetAffx (Affymetrix). Enriched pathways and functions for the subset transcript clusters by class comparison were identified using IPA (Ingenuity).

Quantitative PCR.

Meningeal tissue or FACS-sorted cells were collected in TRIzol (Invitrogen), and total RNA was extracted using PureLink RNA Mini or Micro kits (Life Technologies) per the manufacturer's instructions. Purified RNA was then treated with amplification-grade DNase I (Invitrogen) to remove contaminating DNA and reverse transcribed into cDNA by using an iScript cDNA Synthesis kit (Life Technologies). Real-time PCR was performed using SYBR Green (Applied Biosystems) and cDNA template or water (non-template negative control) at an annealing temperature of 60 degrees with a CFX96 Real-Time PCR machine (Bio-Rad Laboratories). Reactions were conducted in duplicates, and PCR products were subjected to melt analysis to confirm purity after DNA amplification. For each gene, expression values were normalized to a *Actb* (meningeal samples) or 18S (sorted cells) housekeeping genes. The resulting relative gene expression was then expressed relative to the housekeeping gene or as a fold-change from indicated control samples. Primers were designed and obtained from Integrated DNA Technologies (IDT), and sequences are provided in Supplementary Table 4.

Statistical analysis.

Statistical analyses for data for experiments containing two groups were performed using a Student's *t* test or a Mann-Whitney rank sum test. Experiments involving more than two groups were analyzed by ANOVA followed by a Student-Newman-Keuls test or a Holm-Sidak test for pairwise comparisons. All statistical analyses were performed in Graphpad Prism 6.0 or Sigma Plot 11.0. Groups were considered statistically different at a *P* value of <0.05. All data are displayed as the mean ± SEM.

Data availability.

The microarray datasets generated during the current study are available in the NCBI GEO database (accession no. GSE108648). In addition, all primary data that support the findings of this study are available from the corresponding author upon request.

Supplementary Material

Refer to Web version on PubMed Central for supplementary material.

Acknowledgements

The study was supported by the National Institute of Neurological Disorders and Stroke (NINDS), National Institutes of Health (NIH).

References

1. Mowat AM, Scott CL & Bain CC Barrier-tissue macrophages: functional adaptation to environmental challenges. Nat Med 23, 1258–1270 (2017). [PubMed: 29117177]
2. Okabe Y & Medzhitov R Tissue biology perspective on macrophages. Nat Immunol 17, 9–17 (2016). [PubMed: 26681457]
3. Perdiguero EG & Geissmann F The development and maintenance of resident macrophages. Nat Immunol 17, 2–8 (2016). [PubMed: 26681456]
4. Prinz M, Erny D & Hagemeyer N Ontogeny and homeostasis of CNS myeloid cells. Nat Immunol 18, 385–392 (2017). [PubMed: 28323268]
5. Laurent P et al. Immune-Mediated Repair: A Matter of Plasticity. Front Immunol 8, 454 (2017). [PubMed: 28484454]
6. Butler SJ & Bronner ME From classical to current: analyzing peripheral nervous system and spinal cord lineage and fate. Dev Biol 398, 135–146 (2015). [PubMed: 25446276]
7. Song I & Dityatev A Crosstalk between glia, extracellular matrix and neurons. Brain Res Bull 136, 101–108 (2018). [PubMed: 28284900]
8. Haddad-Tovolli R, Dragano NRV, Ramalho AFS & Velloso LA Development and Function of the Blood-Brain Barrier in the Context of Metabolic Control. Front Neurosci 11, 224 (2017). [PubMed: 28484368]
9. Coles JA, Myburgh E, Brewer JM & McMenamin PG Where are we? The anatomy of the murine cortical meninges revisited for intravital imaging, immunology, and clearance of waste from the brain. Prog Neurobiol 156, 107–148 (2017). [PubMed: 28552391]
10. Rua R & McGavern DB Advances in Meningeal Immunity. Trends Mol Med 24, 542–559 (2018). [PubMed: 29731353]
11. Galea I, Bechmann I & Perry VH What is immune privilege (not)? Trends Immunol 28, 12–18 (2007). [PubMed: 17129764]
12. Kipnis J Multifaceted interactions between adaptive immunity and the central nervous system. Science 353, 766–771 (2016). [PubMed: 27540163]
13. Klein RS, Garber C & Howard N Infectious immunity in the central nervous system and brain function. Nat Immunol 18, 132–141 (2017). [PubMed: 28092376]
14. Ransohoff RM Animal models of multiple sclerosis: the good, the bad and the bottom line. Nat Neurosci 15, 1074–1077 (2012). [PubMed: 22837037]
15. Herz J, Filiano AJ, Smith A, Yogev N & Kipnis J Myeloid Cells in the Central Nervous System. Immunity 46, 943–956 (2017). [PubMed: 28636961]
16. Goldmann T et al. Origin, fate and dynamics of macrophages at central nervous system interfaces. Nat Immunol 17, 797–805 (2016). [PubMed: 27135602]
17. Nayak D, Roth TL & McGavern DB Microglia development and function. Annu Rev Immunol 32, 367–402 (2014). [PubMed: 24471431]
18. Roth TL et al. Transcranial amelioration of inflammation and cell death after brain injury. Nature 505, 223–228 (2014). [PubMed: 24317693]
19. Mrdjen D et al. High-Dimensional Single-Cell Mapping of Central Nervous System Immune Cells Reveals Distinct Myeloid Subsets in Health, Aging, and Disease. Immunity 48, 380–395 e386 (2018). [PubMed: 29426702]
20. Ginhoux F, Schultze JL, Murray PJ, Ochando J & Biswas SK New insights into the multidimensional concept of macrophage ontogeny, activation and function. Nat Immunol 17, 34–40 (2016). [PubMed: 26681460]
21. Louveau A et al. Structural and functional features of central nervous system lymphatic vessels. Nature 523, 337–341 (2015). [PubMed: 26030524]
22. Galea I et al. Mannose receptor expression specifically reveals perivascular macrophages in normal, injured, and diseased mouse brain. Glia 49, 375–384 (2005). [PubMed: 15538754]
23. McGavern DB & Kang SS Illuminating viral infections in the nervous system. Nat Rev Immunol 11, 318–329 (2011). [PubMed: 21508982]

24. Kang SS et al. Migration of cytotoxic lymphocytes in cell cycle permits local MHC I-dependent control of division at sites of viral infection. J Exp Med 208, 747–759 (2011). [PubMed: 21464219]
25. Kim JV, Kang SS, Dustin ML & McGavern DB Myelomonocytic cell recruitment causes fatal CNS vascular injury during acute viral meningitis. Nature 457, 191–195 (2009). [PubMed: 19011611]
26. Kang SS & McGavern DB Lymphocytic choriomeningitis infection of the central nervous system. Front Biosci 13, 4529–4543 (2008). [PubMed: 18508527]
27. Emonet SF, Garidou L, McGavern DB & de la Torre JC Generation of recombinant lymphocytic choriomeningitis viruses with trisegmented genomes stably expressing two additional genes of interest. Proc Natl Acad Sci U S A 106, 3473–3478 (2009). [PubMed: 19208813]
28. Moseman EA, Wu T, de la Torre JC, Schwartzberg PL & McGavern DB Type I interferon suppresses virus-specific B cell responses by modulating CD8(+) T cell differentiation. Sci Immunol 1 (2016).
29. Gossa S, Nayak D, Zinselmeyer BH & McGavern DB Development of an immunologically tolerated combination of fluorescent proteins for in vivo two-photon imaging. Sci Rep 4, 6664 (2014). [PubMed: 25322934]
30. Perdiguero EG et al. The Origin of Tissue-Resident Macrophages: When an Erythro-myeloid Progenitor Is an Erythro-myeloid Progenitor. Immunity 43, 1023–1024 (2015). [PubMed: 26682973]
31. Park CG et al. Five mouse homologues of the human dendritic cell C-type lectin, DC-SIGN. Int Immunol 13, 1283–1290 (2001). [PubMed: 11581173]
32. Takahara K et al. Difference in fine specificity to polysaccharides of Candida albicans mannoprotein between mouse SIGNR1 and human DC-SIGN. Infect Immun 80, 1699–1706 (2012). [PubMed: 22331432]
33. Takahara K, Tokieda S, Nagaoka K & Inaba K Efficient capture of Candida albicans and zymosan by SIGNR1 augments TLR2-dependent TNF-alpha production. Int Immunol 24, 89–96 (2012). [PubMed: 22207132]
34. Takahara K et al. C-type lectin SIGNR1 enhances cellular oxidative burst response against C. albicans in cooperation with Dectin-1. Eur J Immunol 41, 1435–1444 (2011). [PubMed: 21400494]
35. Kato C & Kojima N SIGNR1 ligation on murine peritoneal macrophages induces IL-12 production through NFkappaB activation. Glycoconj J 27, 525–531 (2010). [PubMed: 20589530]
36. Koppel EA et al. Specific ICAM-3 grabbing nonintegrin-related 1 (SIGNR1) expressed by marginal zone macrophages is essential for defense against pulmonary Streptococcus pneumoniae infection. Eur J Immunol 35, 2962–2969 (2005). [PubMed: 16134084]
37. Nagaoka K et al. Association of SIGNR1 with TLR4-MD-2 enhances signal transduction by recognition of LPS in gram-negative bacteria. Int Immunol 17, 827–836 (2005). [PubMed: 15908446]
38. Pavlov VA & Tracey KJ The vagus nerve and the inflammatory reflex--linking immunity and metabolism. Nat Rev Endocrinol 8, 743–754 (2012). [PubMed: 23169440]
39. Stein M, Keshav S, Harris N & Gordon S Interleukin 4 potently enhances murine macrophage mannose receptor activity: a marker of alternative immunologic macrophage activation. J Exp Med 176, 287–292 (1992). [PubMed: 1613462]
40. Mosser DM & Edwards JP Exploring the full spectrum of macrophage activation. Nat Rev Immunol 8, 958–969 (2008). [PubMed: 19029990]
41. Linehan SA, Martinez-Pomares L, Stahl PD & Gordon S Mannose receptor and its putative ligands in normal murine lymphoid and nonlymphoid organs: In situ expression of mannose receptor by selected macrophages, endothelial cells, perivascular microglia, and mesangial cells, but not dendritic cells. J Exp Med 189, 1961–1972 (1999). [PubMed: 10377192]
42. Faraco G, Park L, Anrather J & Iadecola C Brain perivascular macrophages: characterization and functional roles in health and disease. J Mol Med (Berl) 95, 1143–1152 (2017). [PubMed: 28782084]
43. Derecki NC et al. Regulation of learning and memory by meningeal immunity: a key role for IL-4. J Exp Med 207, 1067–1080 (2010). [PubMed: 20439540]

44. Derecki NC, Quinnies KM & Kipnis J Alternatively activated myeloid (M2) cells enhance cognitive function in immune compromised mice. Brain Behav Immun 25, 379–385 (2011). [PubMed: 21093578]
45. Italiani P & Boraschi DReactions.p Results Probl Cell Differ 62, 23–43 (2017). [PubMed: 28455704]
46. Scott CL et al. Bone marrow-derived monocytes give rise to self-renewing and fully differentiated Kupffer cells. Nat Commun 7, 10321 (2016). [PubMed: 26813785]
47. van de Laar L et al. Yolk Sac Macrophages, Fetal Liver, and Adult Monocytes Can Colonize an Empty Niche and Develop into Functional Tissue-Resident Macrophages. Immunity 44, 755–768 (2016). [PubMed: 26992565]
48. Gentek R, Molawi K & Sieweke MH Tissue macrophage identity and self-renewal. Immunol Rev 262, 56–73 (2014). [PubMed: 25319327]
49. Misharin AV et al. Monocyte-derived alveolar macrophages drive lung fibrosis and persist in the lung over the life span. J Exp Med 214, 2387–2404 (2017). [PubMed: 28694385]
50. Gundra UM et al. Vitamin A mediates conversion of monocyte-derived macrophages into tissue-resident macrophages during alternative activation. Nat Immunol 18, 642–653 (2017). [PubMed: 28436955]
51. Cronk JC et al. Peripherally derived macrophages can engraft the brain independent of irradiation and maintain an identity distinct from microglia. J Exp Med 215, 1627–1647 (2018). [PubMed: 29643186]
52. Tebruegge M & Curtis N Epidemiology, etiology, pathogenesis, and diagnosis of recurrent bacterial meningitis. Clin Microbiol Rev 21, 519–537 (2008). [PubMed: 18625686]
53. Netea MG et al. Trained immunity: A program of innate immune memory in health and disease. Science 352, aaf1098 (2016). [PubMed: 27102489]
54. Rosas-Ballina M et al. Acetylcholine-synthesizing T cells relay neural signals in a vagus nerve circuit. Science 334, 98–101 (2011). [PubMed: 21921156]
55. Herz J, Johnson KR & McGavern DB Therapeutic antiviral T cells noncytopathically clear persistently infected microglia after conversion into antigen-presenting cells. J Exp Med 212, 1153–1169 (2015). [PubMed: 26122661]
56. Manglani M & McGavern DB Intravital Imaging of Neuroimmune Interactions Through a Thinned Skull. Curr Protoc Immunol 120, 24 22 21–24 22 12 (2018).

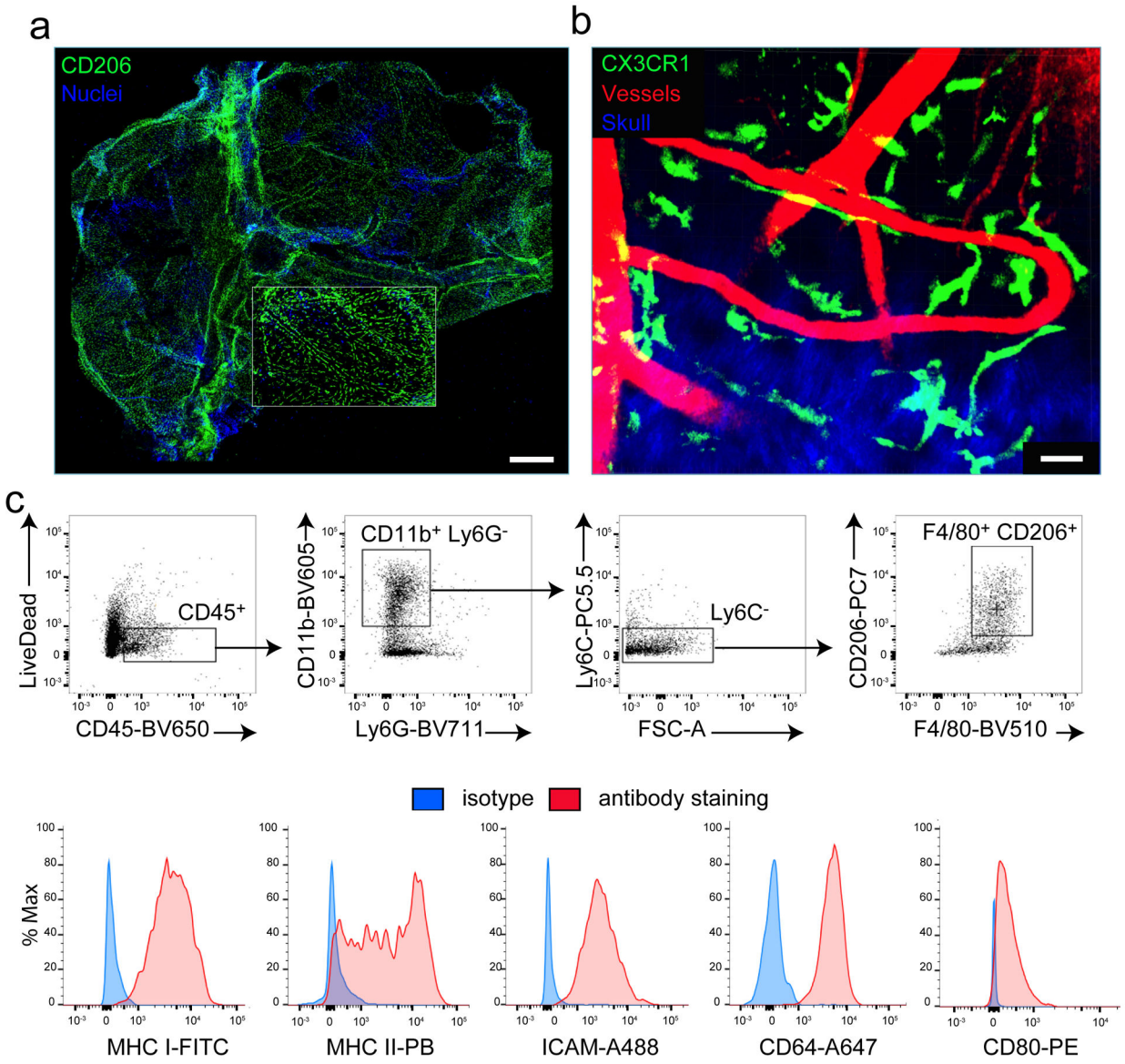

Figure 1. MMs are distributed throughout the meninges under steady state conditions.

(**a**) A representative maximal projection of a confocal *z*-stack shows a meningeal whole mount from a naive B6 mouse. The inset shows a region of the lobe. Image is representative of 5 independent mice. CD206 (green) and DAPI+ nuclei (blue). Scale bar: 1mm. (**b**) A representative maximal projection of a two-photon *z*-stack viewed through a thinned skull of a naive *Cx3cr1*$^{gfp/+}$ mouse shows elongated MMs (green) alongside meningeal vasculature (red) just beneath the skull bone (blue). Image is representative of 4 independent mice. Scale bar: 30μm. (**c**) FACs plots from a naive mouse depict the gating strategy used to analyze cells extracted from digested meninges. Sample were pre-gated on single cells using SSC/FSC signal, after which living (LiveDead^{-}) leukocytes (CD45^{+}) were identified. CD11b^{+} Ly6C^{-} Ly6G^{-} gating was used to exclude neutrophils / inflammatory monocytes, and MMs were identified as being F4/80^{+} CD206^{+}. Histograms depict staining for MHC I (H-2D^{b} H-2K^{b}), MHC II (I-A^{b}/I-E^{b}), ICAM-1, CD64, and CD80 (red) relative to an isotype

control antibody (blue) on gated MMs. Data are representative of three independent experiments with eight mice per group.

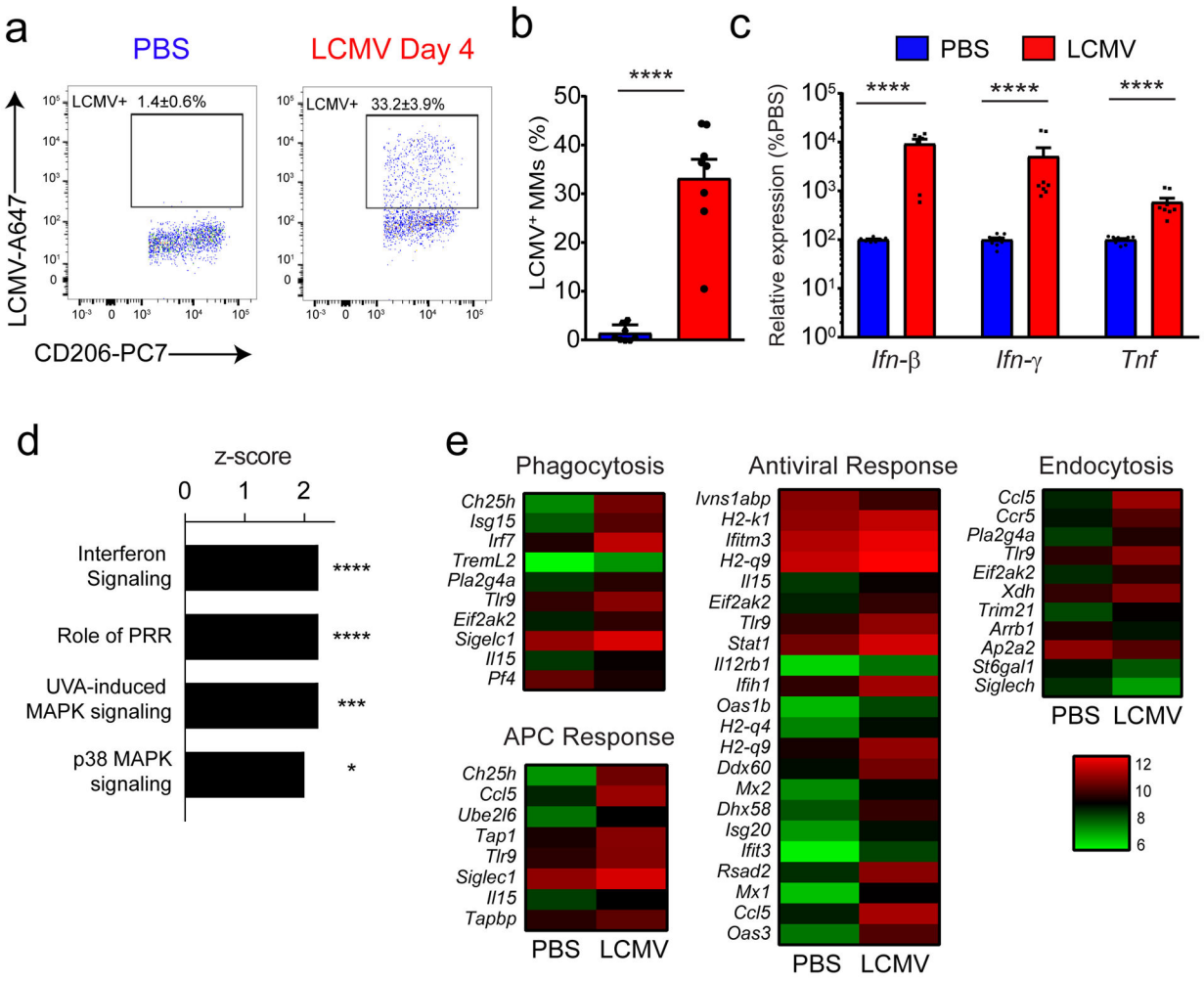

Figure 2. MMs are activated and infected during LCMV meningitis.

(**a,b**) At day 4 following injection of PBS or LCMV, MMs were analyzed flow cytometrically for intracellular LCMV nucleoprotein (NP). Representative FACS plots show the percentage of LCMV-infected MMs (gated on LiveDead$^-$ CD45$^+$ Thy1.2$^-$ CD11b$^+$ Ly6C$^-$ Ly6G$^-$ F4/80$^+$ CD206$^+$ cells) (**a**). Bar graphs show the mean ± SEM for the indicated groups, and asterisks denote statistical significance (****p<0.001, unpaired two-tailed Student's t-test). Data are representative of five independent experiments with eight mice per group (**b**). (**c**) *Ifnb*, *Ifng* and *Tnf* mRNA were quantified by Q-PCR in the meninges of LCMV versus PBS-injected controls at day 2. Bar graphs show the mean ± SEM for the indicated groups, and asterisks denote statistical significance (****p<0.001, two-tailed Mann-Whitney test). Data are representative of 3 independent experiments with nine (PBS) or eight mice (LCMV) per group. (**d-e**) Microarray analysis was performed on RNA extracted from sorted MMs (gated on 7-AAD$^-$ Thy1.2$^-$CD45.2$^+$ CD11b$^+$ Gr1$^-$ F4/80$^+$ CD206$^+$) of LCMV-infected mice at day 4 post-infection and compared to mock-infected mice. Bar graph showing the top four upregulated biological pathways linked to cell signaling in MMs after LCMV infection. Bars represent the z-score, and p-values at the intersections (*p<0.05, ***p<0.001, ****p<0.0001, right-tailed Fisher's exact test using no

multiple comparison correction) are indicated. To enhance the stringency of our analysis, we considered only functions with a *z*-score ≥ 2 or ≤ −2. A complete list is provided in Supplementary Table 1 (‘Enriched_Pathways’ tab). Pattern recognition receptor (PRR); ultra-violet A (UVA); mitogen-activated protein kinase (MAPK) Data are representative of four independent experiments with ninety mice per group (**d**). Heat maps show expression of differentially regulated genes that were statistically different ($p<0.05$, Welch-modified *t*-test under Benjamini–Hochberg (BH) false discovery rate (FDR) multiple comparison correction conditions) from PBS-injected controls and exceeded a threshold of 1.5-fold. Each column depicts the color-coded mean expression of the denoted genes. Genes are clustered together based on functional relatedness. Red and green denotes higher and lower relative expression respectively. See corresponding Supplementary Table 1 (‘Gene_Expression’ tab). Data are representative of four independent experiments with ninety mice per group (**e**).

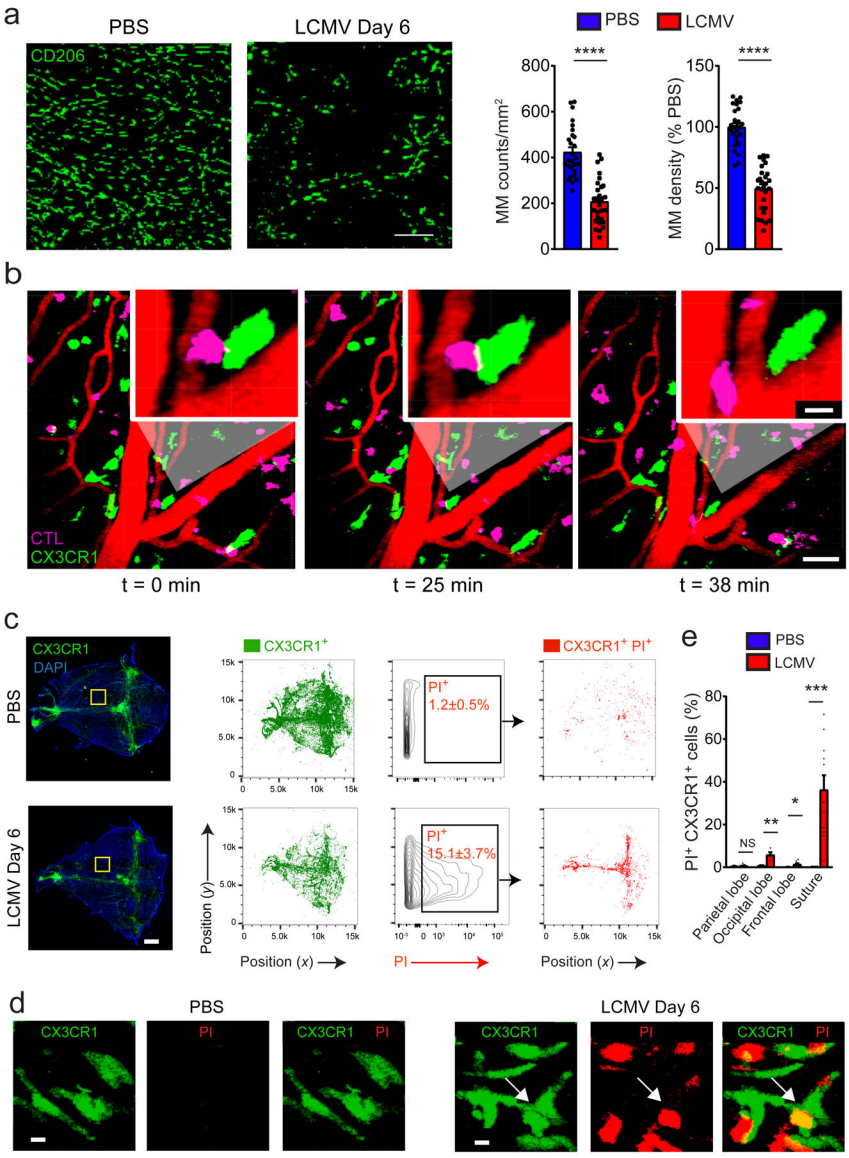

Figure 3. MM numbers diminish at the peak of meningitis.

(**a**) Meningeal whole mount stain of CD206^{+} cells (green) of PBS (left panel) vs. LCMV-injected (middle panel) mice at day 6 and quantification of cell density (right panel). Scale bar: 30μm. The absolute number of MMs and their percent reduction relative to the control group were calculated by histocytometry based on a sampling of the meninges beneath the frontal, parietal, and interparietal bones as well as the lamboid and sagittal sutures. Bar graphs show the mean ± SEM for the indicated groups, and asterisks denote statistical significance (****p<0.001, unpaired two-tailed Student's t test). Data are representative of two independent experiments with twenty-eight regions per group. (**b**) A representative time lapse captured by two-photon microscopy through the thinned skull of a day 6 LCMV-infected *Cx3cr1*$^{gfp/+}$ mouse shows D^{b}GP$_{33–41}$ specific (P14) CTL (pink) interacting with *Cx3cr1*-GFP^{+} macrophages (green) at the denoted time points. Scale bar: 50μm. The insets show a magnified view of an interaction. Scale bar: 10μm. Blood vessels are visualized by

Evans Blue (red). See corresponding Supplementary Video 3. Data are representative of five independent mice. (**c**) Images of meningeal whole mounts (left panels) and corresponding histocytometric plots (middle panels) of the meninges from *Cx3cr1*$^{gfp/+}$ mice 6 days after following injection of PBS or LCMV. Mice were injected i.p. with propidium iodide 1 hour before sacrifice to localize dead cells. *Cx3cr1*-GFP^{+} surfaces (green) were gated and plotted on a separate *xy* axis to quantify the percentage of myeloid cells that were PI^{+}. Percentages of PI^{+} cells are denoted in the black boxes and the anatomical position of these cells (red) is shown in the adjacent plots. Scale bar: 1mm. Data are representative of two independent experiments with two mice per group. (**d**) Magnified images denoted by yellow boxes in (**c**) depict PI^{+} (red) *Cx3cr1*-GFP+ (green) MMs after LCMV infection. Scale bar: 5μm. Data are representative of two independent experiments with four mice per group. (**e**) The bar graph shows the percentage of *Cx3cr1*-GFP^{+} PI^{+} cells in the denoted meningeal regions for PBS vs. LCMV-injected mice at day 6. Graphs show the mean ± SEM for the indicated groups, and asterisks denote statistical significance (*p<0.05, **p<0.01, ***p<0.001, unpaired two-tailed Student's t test). Data are representative of two independent experiments with four (occipital), eight (parietal and frontal) or eleven (suture) regions per group.

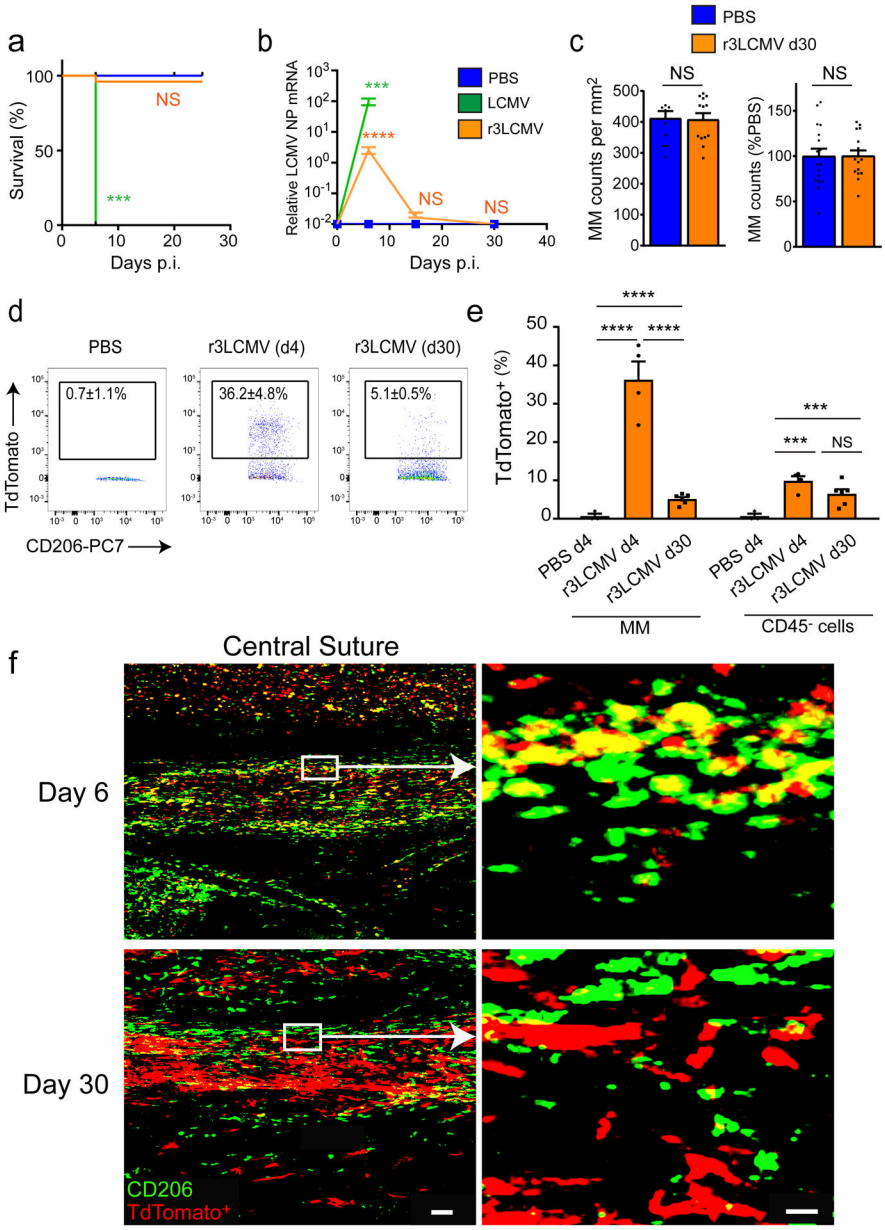

Figure 4. Most infected MMs are cleared and replaced after sub-lethal meningitis.

(**a**) Survival was monitored in mice injected with 1×10^3 PFU of wild type (WT) LCMV Armstrong (green), 1.5×10^4 r3LCMV-teal fluorescent protein (TFP) (orange), or PBS (blue). Mice succumbed to WT LCMV infection but not to r3LCMV-TFP or PBS. Asterisks denote statistical significance (***p<0.001, Kaplan Meier Survival Analysis). Data are representative of four independent experiments with ten (LCMV) or twenty-five (PBS, r3LCMV) mice. (**b**) LCMV RNA levels were quantified at days 0, 6, 15, and 30 post-infection and compared to mock-infected mice. LCMV-NP RNA levels were significantly higher than controls for both viruses at day 6 post-infection, but not at later timepoints. Mice infected with WT LCMV did not survive past day 6. Graphs show the mean ± SEM for the indicated groups, and asterisks denote statistical significance (NS, not significant;

p<0.001; ****p<0.0001; unpaired two-tailed Student's t test). Data are representative of two (PBS) and four (LCMV, r3LCMV) independent experiments with four (PBS) and eight (LCMV, r3LCMV) mice per group. (**c**) At day 30 post-infection, the number or frequency of $CD206^+$ MMs was quantified by histocytometry in meningeal whole mounts (left graph) or by flow cytometry using meningeal cell suspensions (right graph) and compared to mock-infected controls (NS, not significant). Data are representative of two independent experiments with ten (PBS) or thirteen (r3LCMV) regions (left graph) or four independent experiments with seventeen (PBS) and sixteen (r3LCMV) mouse. (**d,e**) $Stop^{fl/fl}$ TdTomato mice were infected with r3LCMV-iCre. At days 4 and 30, infected MMs and their progeny were analyzed flow cytometrically. Representative FACS plots show the percentage (inside black boxes) of $TdTomato^+$ MMs (gated on $LiveDead^-$ $CD45^+$ $Thy1.2^-$ $CD11b^+$ $Ly6C^-$ $Ly6G^-$ $F4/80^+$ $CD206^+$ cells). Data are representative of two independent experiments with four (day 4) or six (day 30) mice (**d**). The bar graph shows the frequency of $TdTomato^+$ MMs (gated on $LiveDead^-$ $CD45^+$ $Thy1.2^-$ $CD11b^+$ $Ly6C^-$ $Ly6G^-$ $F4/80^+$ $CD206^+$ cells) vs. $CD45^-$ stromal cells at day 4 and 30 post-infection analyzed by flow cytometry. Asterisks denote statistical significance (p<0.001, ****p<0.0001, NS=not significant; unpaired two-tailed Student's t test). Data are representative of two independent experiments with four (day 4) or six (day 30) mice (**e**). (**f**) Representative maximal projections of confocal z-stacks show meningeal whole mount images from $Stop^{fl/fl}$ TdTomato mice 6 and 30 days after r3LCMV infection. The central suture runs along the middle of each image. Scale bar: 100μm. The insets (white box) show an overlap of CD206 (green) and TdTomato (red) at day 6, but not at day 30. Data are representative of 3 mice. Scale bar: 20μm.

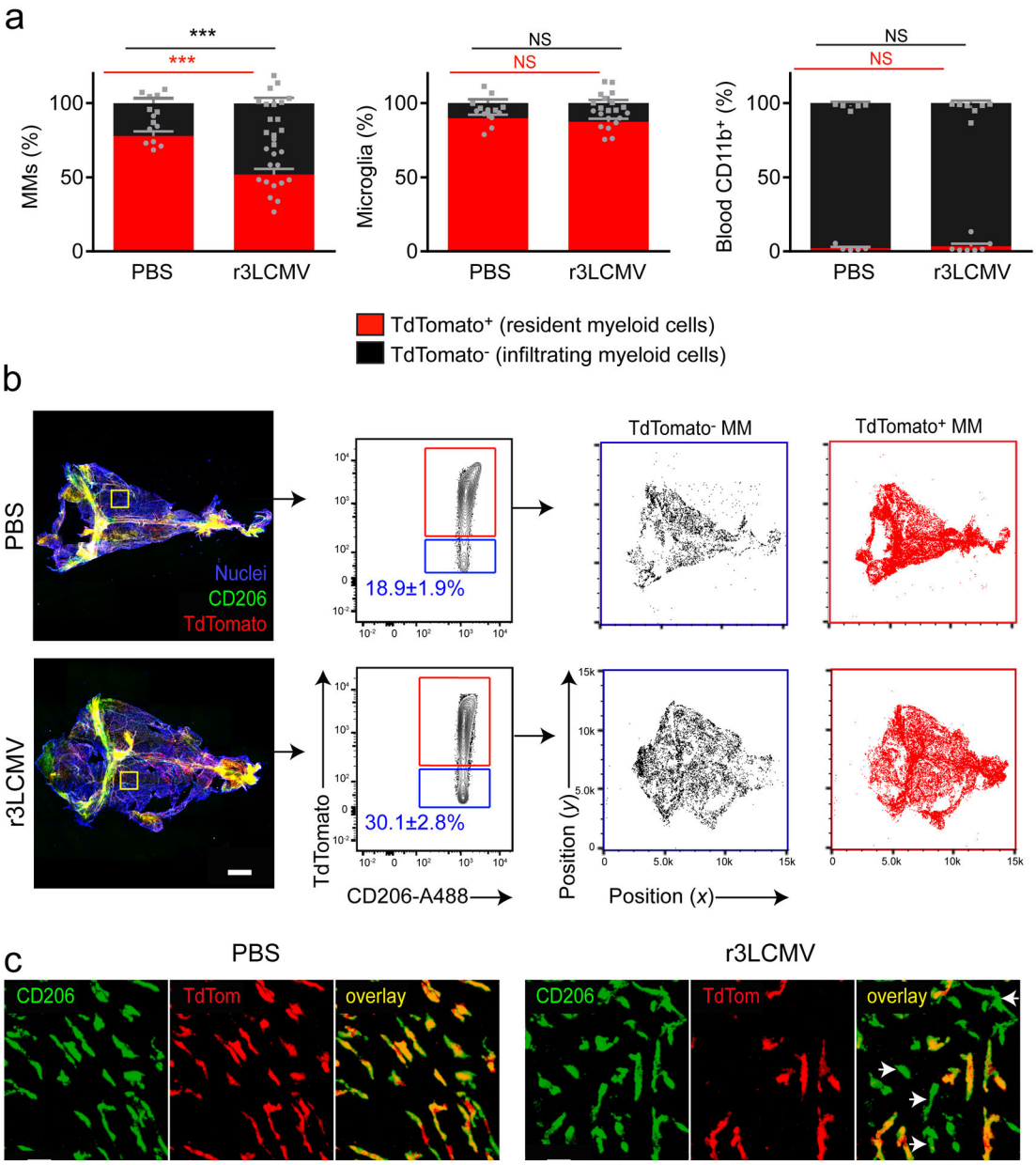

Figure 5. Meningitis drives long-term engraftment of blood monocytes into the meninges.

(**a**) At day 30, MMs (gated on LiveDead$^-$ CD45$^+$ Thy1.2$^-$ CD11b$^+$ Ly6C$^-$ Ly6G$^-$ F4/80$^+$ CD206$^+$ cells), brain microglia (gated on LiveDead$^-$ CD45$^+$ CD11b$^+$ Thy1.2$^-$ Ly6C$^-$ Ly6G$^-$ CD206$^-$ cells) and blood myeloid cells (gated on LiveDead$^-$ CD45$^+$ CD11b$^+$ Thy1.2$^-$) were analyzed flow cytometrically and compared to mock-infected controls. The proportion of TdTomato$^-$ cells is significantly increased in the MM compartment (***p<0.001; unpaired two-tailed Student's *t* test), but not in blood monocytes or microglia (NS, not significant; unpaired two-tailed Student's *t* test) from r3LCMV-TFP infected mice. Bar graphs show the mean ± SEM for the indicated groups. Data are representative of four independent experiments with seven and fourteen mice per group (MM), seven and eleven mice per group (Microglia), five and seven mice per group (blood), respectively for PBS and LCMV

groups. (**b**) Representative maximal projection of meningeal whole mounts (left panels) depict CD206 (green) and Tdtomato (red) expression in PBS- vs. r3LCMV-injected mice at day 30. $CD206^{+}$ surfaces were analyzed by histocytometry and gated based on TdTomato+ channel intensity (red boxes). $CD206^{+}TdTomato^{+}$ and $CD206^{+}TdTomato^{-}$ cells were plotted on an *xy* coordinate scale to identify their anatomical distribution on meningeal whole mounts. Data are representative of two independent experiments with six mice. Scale bar: 500μm. (**c**) Magnified images denoted by yellow boxes in (**b**) show $CD206^{+}$ $TdTom^{-}$ MMs (white arrow heads) after r3LCMV infection. Scale bar: 50μm.

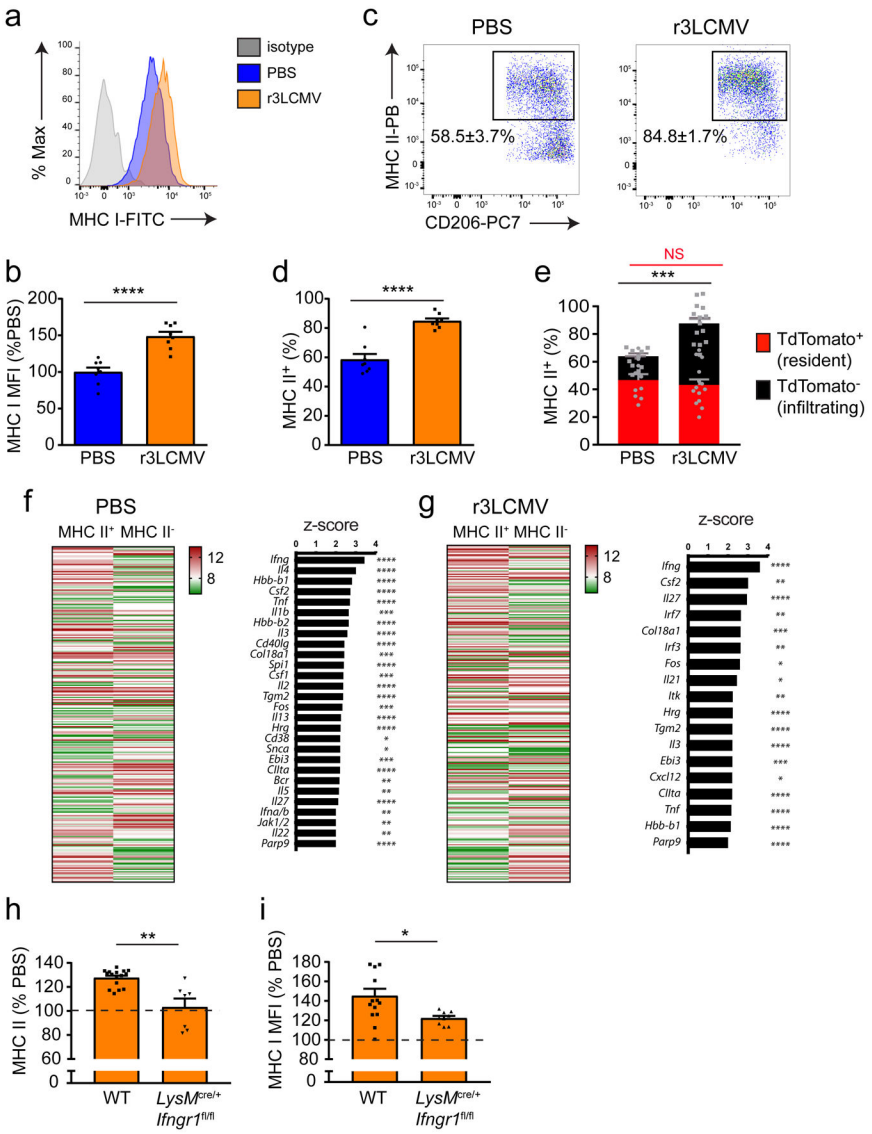

Figure 6. IFNγ promotes engraftment of the meninges by peripheral MHC II$^+$ cells.

(**a-d**) At day 30 post infection, MMs (gated on LiveDead$^-$ CD45$^+$ Thy1.2$^-$ CD11b$^+$ Ly6C$^-$ Ly6G$^-$ F4/80$^+$ CD206$^+$ cells) were analyzed flow cytometrically for MHC I (**a,b**) and MHC II (**c,d**) expression and compared to mock-infected controls. Representative FACS plots (**a,c**) and the corresponding bar graphs (**b,d**) demonstrate a statistically significant increase in MHC I and MHC II levels on MMs from mice previously infected with r3LCMV relative to the mock-infected control group. Bar graphs show the mean ± SEM for the indicated groups, and asterisks denote statistical significance (****p<0.0001, unpaired two-tailed Student's t test). Data are representative of two independent experiments with eight mice per group. (**e**) A similar experiment was performed using *Cx3cr1*$^{CreER/+}$ x Stop$^{fl/fl}$ TdTomato mice. Bar graphs show the mean ± SEM for the indicated groups, and asterisks denote statistical significance. In day 30 r3LCMV-infected mice, a significant increase was observed in the proportion of MHC II$^+$ TdTomato$^-$ cells (infiltrating myeloid cells) (***p<0.01; unpaired two-tailed Student's t test), but not MHC II$^+$ TdTomato$^+$ cells (NS, not significant; unpaired

two-tailed Student's *t* test). Meningeal macrophages were gated on LiveDead^{-} CD45^{+} Thy1.2^{-} CD11b^{+} Ly6C^{-} Ly6G^{-} F4/80^{+} CD206^{+} cells. Data are representative of four independent experiments with ten (PBS) and fourteen (r3LCMV) mice per group. (**f,g**) Microarray analysis was performed on RNA extracted from sorted MHC II^{+} MMs of mice injected with PBS (**f**) and LCMV (**g**) 30 days prior and compared to MHC II^{-} MMs. Data are representative of four independent experiments with ninety mice per group. Meningeal macrophages were gated on LiveDead^{-} Thy1.2^{-} CD45.2^{+} CD11b^{+} Ly6C^{-} Ly6G^{-} F4/80^{+} CD206^{+} and I-A^{b}/I-E^{b} positive (MHC II^{+} MM) or I-A^{b}/I-E^{b} negative (MHC II^{-} MM). Heat maps in **f** and **g** depict differentially regulated genes between MHC II^{+} vs. MHC II^{-} MMs (p<0.05, Welch-modified *t*-test under BH FDR multiple comparison correction conditions; greater than 1.5-fold). Each column shows color coded mean relative expression levels. See corresponding Supplementary Table 2. Bar graphs in **f** and **g** depict the top upstream regulators of the gene expression patterns in MHC II^{+} vs. MHC II^{-} MM. Bars represent *z*-scores, and p-values at the intersections (*p<0.05, **p<0.01, ***p<0.001, ****p<0.0001, right-tailed Fisher's exact test using no multiple comparison correction) are indicated. Only *z*-scores ≥ 2 or ≤ −2 were plotted. For a complete list of differentially regulated genes see Supplementary Table 2 ('Gene_Expression_PBS' and 'MHC II^{+}_upstream_regulatorsPBS' tabs for mock-infected mice; 'Gene_Expression_LCMV' and 'MHC II $^{+}$_upstream_regulatorsLCMV' tabs for the r3LCMV-infected mice). (**h,i**) At day 30 post-r3LCMV infection, MMs from littermate wild type (WT) vs. *LysM*$^{Cre/+}$ x *Ifngr1*$^{fl/fl}$ mice were analyzed flow cytometrically for MHC II (**h**) and MHC I (**i**) expression and compared to mock-infected mice. MMs were gated on LiveDead^{-} Thy1.2^{-}CD45.2^{+} CD11b^{+} Ly6C^{-} Ly6G^{-} F4/80^{+} CD206^{+}. Data are represented as a percentage relative to mock-infected control mice. (*p<0.05, **p<0.01; unpaired two-tailed Student's *t* test). Bar graphs show the mean ± SEM for the indicated groups, and the dashed line represents the mock-infected control. Data are representative of five independent experiments with sixteen (WT) and seven (*LysM*$^{Cre/+}$ x *Ifngr1*$^{fl/fl}$) mice per group (MHC II) or fourteen (WT) and nine (*LysM*$^{Cre/+}$ x *Ifngr1*$^{fl/fl}$) mice per group (MHC I).

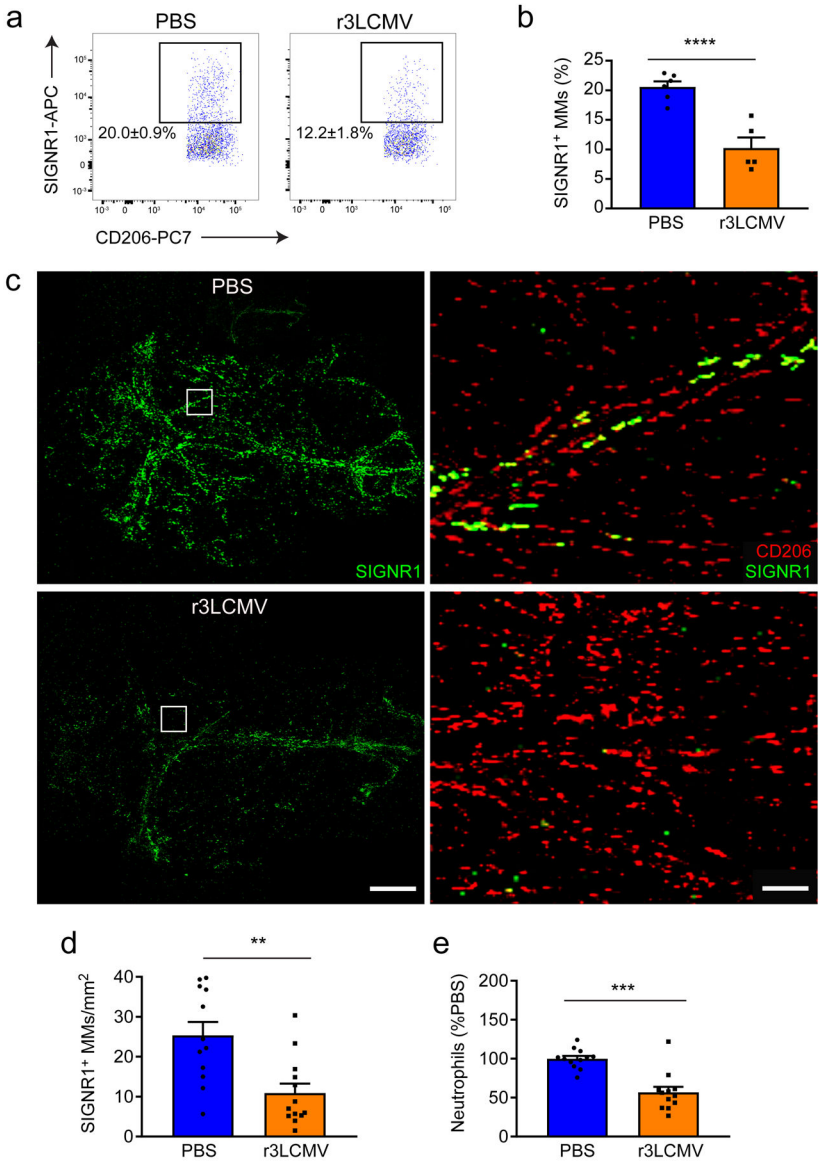

Figure 7. Long-term alteration of MM sensome after infection.

(**a,b**) At day 30 post infection, MMs (gated on LiveDead$^-$ CD45$^+$ Thy1.2$^-$ CD11b$^+$ Ly6C$^-$ Ly6G$^-$ F4/80$^+$ CD206$^+$ cells) were analyzed flow cytometrically for SIGN-R1 expression and compared to mock-infected controls. Representative FACS plots (**a**) and corresponding bar graphs (**b**) show a statistically significant decrease in SIGN-R1 levels on MMs from day 30 r3LCMV-infected mice relative to mock-infected controls (****p<0.0001; unpaired two-tailed Student's *t* test). Bar graphs show the mean ± SEM for the indicated groups. Data are representative of two independent experiments with six (PBS) and five (LCMV) mice per group. (**c**) Maximal projections of meningeal whole mounts from PBS- vs. r3LCMV-injected mice at day 30 show CD206 (red) and SIGN-R1 (green) expression. Scale bar: 1mm. Magnified areas highlighted with white boxes are shown in the left panels. Scale bar: 50μm. (**d**) CD206$^+$ MMs on meningeal whole mounts were analyzed by histocytometry and quantified for SIGN-R1 expression. The density of CD206$^+$SIGN-R1$^+$ cells was

significantly reduced 30 days after a r3LCMV infection relative to the control group (**p<0.01, unpaired two-tailed Student's *t* test). Bar graphs show the mean ± SEM for the indicated groups. Data are representative of two independent experiments with twelve (PBS) and thirteen (LCMV) mice per group. (**e**) Six hours after i.c. LPS challenge, the number of neutrophils (gated on LiveDead^{-} CD45^{+} Thy1.2^{-} CD11b^{+} Ly6C^{-} Ly6G^{+} cells) that infiltrated the meninges of day 30 r3LCMV- relative to mock-infected controls was quantified by flow cytometry. Data are represented as a percentage of the mock-infected group (*p<0.05, unpaired two-tailed Student's *t* test). Bar graphs show the mean ± SEM for the indicated groups. Data are representative of three independent experiments with twelve mice per group.

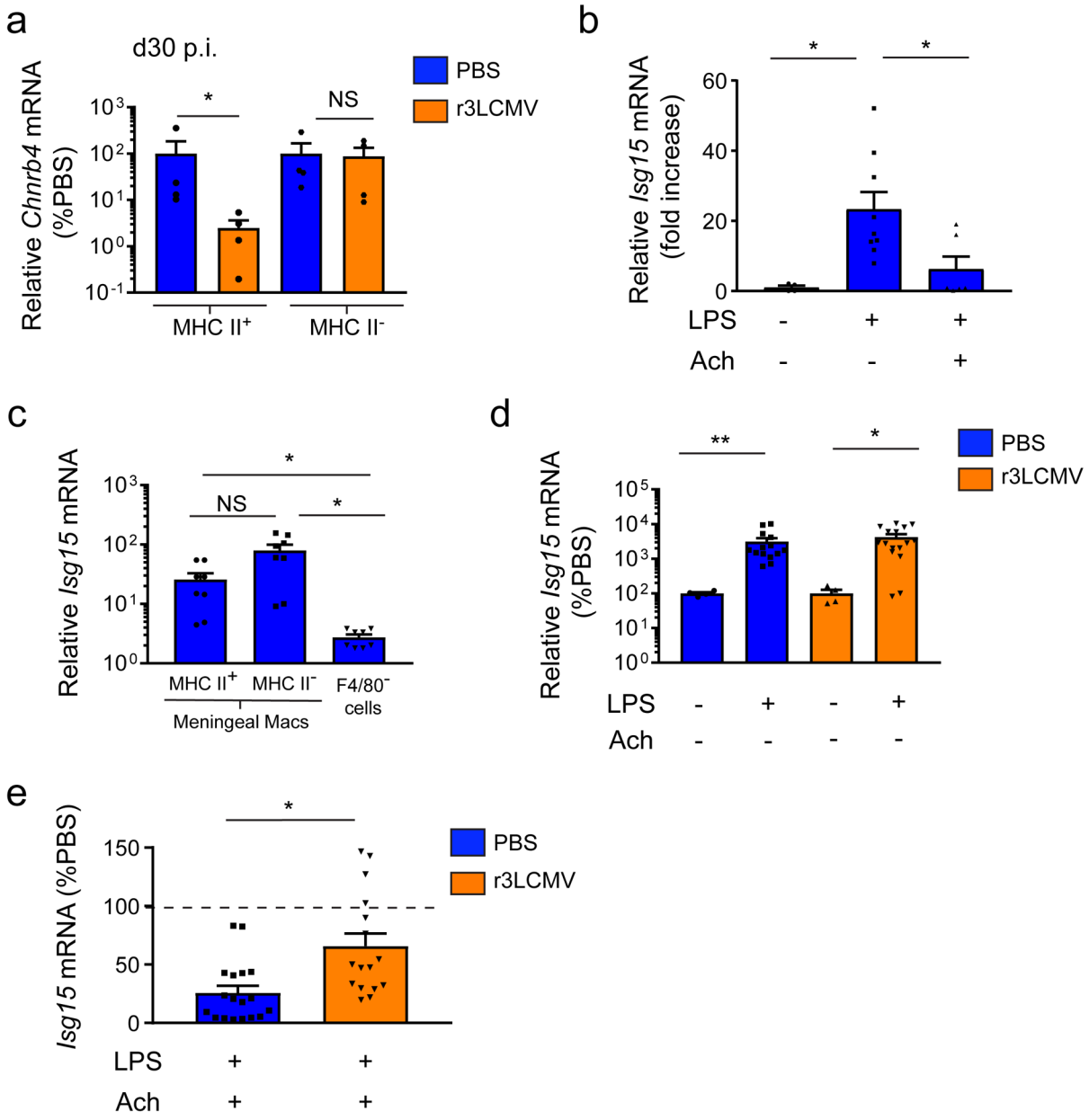

Figure 8. MMs fail to quench inflammatory reactions following meningitis.

(**a**) Thirty days following infection with r3LCMV, MHC II$^+$ and MHC II$^-$ MMs were sorted and RNA was extracted to quantify Chnrb4 mRNA levels by Q-PCR. MMs were sorted based on the following markers: LiveDead$^-$ Thy1.2$^-$ CD45.2$^+$ CD11b$^+$ Ly6C$^-$ Ly6G$^-$ F4/80$^+$ CD206$^+$ and I-A^b/I-E^b positive (MHC II$^+$ MM) or I-A^b/I-E^b negative (MHC II$^-$ MM). Compared to mock-infected mice, MHC II$^+$ macrophages showed a significant decrease in Chnrb4 expression. Bar graphs show the mean ± SEM for the indicated groups, and asterisks denote statistical significance (*p<0.05, NS, not significant; two-tailed Mann-Whitney test). Data are representative of four independent experiments with ninety mice per

group. (**b**) Meningeal ISG15 mRNA levels were quantified by Q-PCR in naïve B6 mice 3 hours after i.p. LPS challenge. Mice also received a transcranial hydrogel containing acetylcholine or a vehicle control. Expression data are represented as a fold-expression over the control group, which did not receive LPS or the hydrogel. Bar graphs show the mean ± SEM for the indicated groups, and asterisks denote statistical significance (*$p<0.05$, one-way ANOVA followed by Holm-Sidak pairwise comparison test). Data are representative of two independent experiments with four (LPS- Ach-), nine (LPS+ Ach-) and six (LPS+ Ach +) mice per group. (**c**) Three hours after an i.p. LPS challenge, meninges were extracted and three cell populations were sorted (MHC II^+ MM, MHC II^- MMs and residual $F4/80^-$ cells) to extract mRNA and quantify ISG15 expression by Q-PCR. MMs both express ISG15 following LPS challenge. Bar graphs show the mean ± SEM for the indicated groups, and asterisks denote statistical significance (*$p<0.05$, one-way ANOVA on ranks followed by two-tailed Student-Newman-Keuls pairwise comparison test). Data are representative of four independent experiments with eight samples pooled from ten mice per group. (**d**) Thirty days after infection with r3LCMV-TFP, mice were challenged i.p. with LPS or PBS, and meningeal ISG15 mRNA levels were quantified and compared to mock-infected mice. Bar graphs show the mean ± SEM for the indicated groups, and asterisks denote statistical significance (*$p<0.05$, **$p<0.01$; Mann Whitney two-tailed test). Data are representative of two independent experiments with four (LPS- Ach- PBS), fourteen (LPS+ Ach- PBS), four (LPS- Ach- LCMV) and sixteen (LPS+ Ach- r3LCMV) mice per group. (**e**) Thirty days after infection with r3LCMV-TFP, mice received an acetylcholine- or vehicle-containing hydrogel and were subsequently challenged with i.p. LPS. Meningeal ISG15 mRNA was then quantified by Q-PCR, and ISG15 expression levels in the presence of acetylcholine were graphed relative to the vehicle hydrogel control group as a percent induction. Bar graphs show the mean ± SEM for the indicated groups, and asterisks denote statistical significance (*$p<0.05$, Mann-Whitney two-tailed test). Data are representative of four independent experiments with eighteen (PBS) and sixteen (LCMV) mice per group.